Preprint typeset using LaTeX style emulateapj v. 5/2/11

SPECTROSCOPIC CONFIRMATION OF THE RICH $Z = 1.80$ GALAXY CLUSTER JKCS 041 USING THE WFC3 GRISM: ENVIRONMENTAL TRENDS IN THE AGES AND STRUCTURE OF QUIESCENT GALAXIES

Andrew B. Newman[1,2], Richard S. Ellis[1], Stefano Andreon[3], Tommaso Treu[4], Anand Raichoor[3,5], and Ginevra Trinchieri[3]

ABSTRACT

We present *Hubble Space Telescope* imaging and grism spectroscopy in the field of the distant galaxy cluster JKCS 041 using the Wide Field Camera 3. Our survey yields 98 grism redshifts whose precision is typically ∼20 times better than photometric estimates. We confirm that JKCS 041 is a rich cluster and derive a redshift $z = 1.80$ via the spectroscopic identification of 19 member galaxies, of which 15 are quiescent. The spatial distribution of confirmed members is centered upon the diffuse X-ray emission seen by the *Chandra* observatory. As JKCS 041 is the most distant known cluster with such a large and spectroscopically-confirmed quiescent population, it provides an unique opportunity to study the effect of the environment on galaxy properties seen at early epochs. We construct high-quality composite spectra of the confirmed quiescent members that reveal prominent Balmer and metallic absorption lines. From these, we infer that the more massive members ($M_* > 10^{11}\,M_\odot$) have a mean stellar age of $1.4^{+0.3}_{-0.2}$ Gyr, whereas lower-mass examples ($M_* = 10^{10.5-11}\,M_\odot$) have a younger mean age of $0.9^{+0.2}_{-0.1}$ Gyr. These ages agree remarkably closely with those inferred by Whitaker et al. for similarly-selected quiescent galaxies in the field, supporting the idea that the cluster environment is more efficient at truncating star formation while not having a strong effect on the mean epoch of quenching. In contrast to field samples, there is no sign of low-level Hβ or [O III] emission in the composite spectra of the quiescent cluster members. By comparing the ellipticity distribution of these galaxies to a large sample of coeval field galaxies drawn from the CANDELS survey, we find some evidence (90% confidence) for a lower fraction of disk-like quiescent systems in JKCS 041. Taking this into account, we do not detect a significant difference between the mass–radius relations of the quiescent JKCS 041 members and our $z \sim 1.8$ field sample. We review claims of environmentally-dependent size growth of $z > 1$ quiescent galaxies, and we demonstrate how differences in the morphological mixture of quenched systems may complicate direct comparisons of sizes in different environments.

Subject headings: galaxies: clusters: individual (JKCS 041) — galaxies: elliptical and lenticular, cD — galaxies: evolution — galaxies: high-redshift

1. INTRODUCTION

The evolution of the structure and stellar populations of massive galaxies at high redshifts entails some of the key puzzles in galaxy evolution. The mean size of quiescent galaxies increases by a factor of about 4 since $z = 2.5$ (e.g., Buitrago et al. 2008; van Dokkum et al. 2008; Toft et al. 2009; Williams et al. 2011; Damjanov et al. 2011; Newman et al. 2012), as reflected in a progressive buildup of light in their outer envelopes (van Dokkum et al. 2010), while the typical morphologies of the massive examples appear to become more spheroid-dominated (van der Wel et al. 2011; Chang et al. 2013a,b). At the same time, star formation is being truncated in many galaxies as they transition onto the red sequence. Both the rates of structural growth and the increase in number density of quenched galaxies appear to accelerate at $z \gtrsim 1.5$ (Newman et al. 2012, hereafter N12).

The physical mechanisms driving these changes are only partially understood. Accretion of material in low-mass, gas-poor satellites has emerged as a popular explanation for the structural changes, since this adds stars at large radii while increasing the overall mass comparatively little (e.g., Naab et al. 2009; Bezanson et al. 2009; Hopkins et al. 2009). However, the observed (N12) and theoretical (Nipoti et al. 2012) rates of such minor mergers appear too low to account fully for the rate of size growth, suggesting that additional processes may be at play. The continual arrival of new galaxies onto the red sequence whose sizes may differ from those of the older population already in place further complicates the interpretation; this could lead to a type of progenitor bias whose significance is still debated observationally (e.g., N12; Whitaker et al. 2012; Carollo et al. 2013; Poggianti et al. 2013). Whether a stochastic merger history can lead to the tight scaling relations seen locally has also been questioned by some authors (e.g., Nipoti et al. 2009; Nair et al. 2010).

Additional insight into the growth mechanisms arises from lookback studies that compare the rates of structural evolution as a function of environment. It is expected that the merger history of a galaxy depends on the local density or halo mass (McIntosh et al. 2008;

Email: anewman@obs.carnegiescience.edu
[1] Cahill Center for Astronomy and Astrophysics, California Institute of Technology, MS 249-17, Pasadena, CA 91125, USA
[2] Current Address: The Observatories of the Carnegie Institution for Science, 813 Santa Barbara St., Pasadena, CA 91101
[3] INAF-Osservatorio Astronomico di Brera, via Brera 28, 20121, Milano, Italy
[4] Department of Physics, University of California, Santa Barbara, CA 93106, USA
[5] GEPI, Observatoire de Paris, 77 av. Denfert Rochereau, 75014 Paris, France

Fakhouri et al. 2010; Lin et al. 2010; Jian et al. 2012; Kampczyk et al. 2013). If size growth is primarily merger driven, it is natural to expect that it will proceed at a rate that depends on past merger activity. Internally-driven growth processes such as expansion via mass loss (Fan et al. 2008, 2010; Damjanov et al. 2009), on the other hand, should be less sensitive to environment. At the same time as gradual size growth proceeds, morphological transformations occur through a variety of processes that are both environmentally-related (e.g., mergers, galaxy harassment, tidal interactions, and gas deprivation; see Treu et al. 2003; Moran et al. 2007, and references therein) and internally-driven (e.g., secular bulge growth; Kormendy & Kennicutt 2004). Lookback studies to $z \sim 0.5 - 1$ have been essential to determine the history of morphological change in clusters (e.g., Dressler et al. 1997; Postman et al. 2005; Poggianti et al. 2009).

Similarly, while the cessation of star formation is clearly influenced by both environmentally-related processes — e.g., ram-pressure stripping, gas starvation, galaxy–galaxy interactions — as well as internal mechanisms, such as feedback from supernovae or an active galactic nucleus (AGN), the underlying physical processes and their relative importance as a function of mass and cosmic time remain uncertain. Understanding the history of star formation quenching in different environments aids in disentangling the influence of these processes. Observationally, this is constrained by the evolution of the fraction of quenched galaxies and their star-formation histories in clusters, groups, and the field (e.g., Muzzin et al. 2012; Raichoor & Andreon 2012; Dressler et al. 2013).

High-redshift galaxy clusters represent excellent laboratories in which to address these questions, since they probe extreme overdensities at the epoch when quiescent galaxy growth and also the buildup of the red sequence appear most rapid. The expected decline in the number of clusters at high redshifts, coupled with the increasing difficultly of the observations necessary to locate and confirm them, has limited our knowledge of these systems. To date, only a handful of $z > 1.6$ clusters hosting red galaxies are known (e.g., Papovich et al. 2010; Gobat et al. 2013; Stanford et al. 2012; Zeimann et al. 2012; Muzzin et al. 2013; Tanaka et al. 2013; Galametz et al. 2013, see §7). Spectroscopic data is required not only to confirm a putative cluster and isolate its members but also to precisely constrain the stellar populations and past star formation activity. Very few red cluster galaxies have been spectroscopically studied thus far, which has been the prime limiting factor in undertaking a study of the role of the environment in their evolution.

In this paper we present imaging and grism spectroscopy for the cluster candidate JKCS 041 using the Wide Field Camera 3 (WFC3) onboard the *Hubble Space Telescope* (*HST*). JKCS 041 was originally discovered as an overdensity of galaxies with similar colors (Andreon et al. 2009) in images from the UKIRT Infrared Deep Sky Survey (Lawrence et al. 2007). It exhibits a tight red sequence coincident with diffuse X-ray emission (Andreon & Huertas-Company 2011; Andreon 2011) detected securely in a 75 ks *Chandra* observation. The X-ray gas temperature indicates a high halo mass of $M_{500} = 2.9^{+3.8}_{-2.4} \times 10^{14}\,\mathrm{M}_\odot$ (Andreon et al. 2009). Estimates of the redshift based on different photometric techniques and data sets ranged from $z = 1.9-2.2$. However, earlier attempts to confirm the reality of the cluster and to secure its spectroscopic redshift were unsuccessful.

Here we use the WFC3 grisms to show that JKCS 041 is a genuine $z = 1.80$ rich cluster, confirmed via the spectroscopic confirmation of 19 member galaxies, of which 15 are quiescent. This is by far the largest number of quiescent cluster members beyond $z \simeq 1.5$ with spectroscopic data, making JKCS 041 an unique probe of early evolution in a dense environment. Our observations provide an ideal complement recent *HST* field surveys based on similar WFC3 data, such as CANDELS (Grogin et al. 2011; Koekemoer et al. 2011) and 3D-HST (Brammer et al. 2012).

After describing our observations and methods in Sections 2 and 3, we introduce the cluster members and their basic properties in Section 4. In Section 5, we construct composite spectra of the quiescent cluster members. The stacking technique has been successfully employed in many cluster studies at lower redshifts (e.g., Dressler et al. 2004; Gobat et al. 2008; Poggianti et al. 2009; Muzzin et al. 2012) to discern variations in galaxy populations and star-formation histories with mass and environment. For the first time in such a distant cluster, the quality of our spectra is sufficient to measure age-sensitive stellar absorption features and derive mean stellar ages as a function of galaxy mass. Additionally, through a comparison with composite spectra assembled by Whitaker et al. (2013) based on 3D-HST data, we are able to compare the stellar ages of quenched galaxies in JKCS 041 and the field near the same epoch. We demonstrate that although the fraction of quiescent systems in the cluster is elevated, the mean ages of these galaxies do not differ appreciably from the field sample.

To investigate the role of the environment in structural evolution, in Section 6 we compare the shapes, sizes, and radial mass profiles of members of JKCS 041 to a large sample of coeval field galaxies drawn from the CANDELS survey. By comparing the distribution of axis ratios, we find some evidence that a lower fraction of quiescent galaxies in the cluster contain a significant disk-like component. We consider the effect that variations in the morphological mixture of quenched galaxies in different environments may have on comparisons of the mass–radius relation, and conclude that there is no significant difference in the sizes of the JKCS 041 members compared to the field sample, particularly when these are better matched in morphology. In Section 7 we compare to results derived in other $z > 1.6$ clusters. We discuss the physical significance of our findings in Section 8, and finally summarize them in Section 9.

Throughout we adopt a ΛCDM cosmology with $\Omega_m = 0.3$, $\Omega_\Lambda = 0.7$, and $H_0 = 70$ km s^{-1} Mpc^{-1}. All magnitudes are in the AB system, and stellar masses refer to a Salpeter (1955) initial mass function (IMF).

2. *HST* OBSERVATIONS AND DATA REDUCTION

We observed JKCS 041 with the infrared channel of WFC3 (GO 12927, Cycle 20, P.I. Newman) in four visits with a common pointing center but various spacecraft orientations. One two-orbit visit was devoted to imaging in the F160W and F105W filters, and the remaining 14 orbits were divided among 3 visits comprising G141

and G102 grism observations. In addition to our new *HST* data, JKCS 041 benefits from an array of earlier ground- and space-based photometry. In this section we describe our reduction of the *HST* observations and construction of a multi-wavelength catalog.

2.1. *HST Imaging*

JKCS 041 was imaged through the F160W and F105W filters for approximately 4/3 and 2/3 orbits, respectively, using a four-point dither pattern identical to that adopted by the CANDELS survey (Koekemoer et al. 2011). After combining these deeper exposures with the grism pre-images, described below, the total exposure times were 4.5 ks in F160W and 2.7 ks in F105W. Although the calibrated frames produced using `calwfc3` by the archive on-the-fly pipeline were mostly sufficient, we found it necessary to expand the pixel mask to include additional warm and hot pixels. The exposures were then registered and combined using `multidrizzle` with a pixel scale of $0\farcs06$.

2.2. *Photometric Catalog*

In addition to the new *HST* imaging, JKCS 041 has been observed in the $ugrizJHKs$ filters by the MegaCam and WIRCam instruments at the Canada–France–Hawaii Telescope (CFHT) as part of the CFHT Legacy Survey (Deep Field 1) and the WIRCam Deep Survey (WIRDS; Bielby et al. 2012). We also made use of *Spitzer* Infrared Array Camera (IRAC) observations in the 3.6μm and 4.5μm channels taken as part of the Spitzer Wide-Area Infrared Extragalactic Survey (SWIRE; P.I. Lonsdale).

A multi-wavelength catalog was created using `SExtractor` (Bertin & Arnouts 1996) with F160W as the detection band. The procedures followed those detailed in N12. All images were first aligned and drizzled onto the F160W pixel scale. Colors were then measured in apertures on images of matched resolution. To account for systematic uncertainties in zeropoints and PSF matching, we added a 3% uncertainty (10% for IRAC) in quadrature to the random flux errors. For a few of the galaxies that we confirm to be members of JKCS 041 (IDs 359, 375, 376, and 281; see Section 4.1), the aperture photometry was affected by neighboring sources. In order to measure accurate colors in these cases, we used `Galfit` (Peng et al. 2002) to fit Sérsic profiles to all nearby sources simultaneously in each observed band.

Photometric redshifts $z_{\rm phot}$ were computed using the z_p estimator provided by `EAZY` (Brammer et al. 2008). Stellar population parameters were derived using a custom code for the sample of bright galaxies with strong continuum signal in the grism spectra (see Section 3.2). For fainter galaxies, we used `FAST` (Kriek et al. 2009) to fit Bruzual & Charlot (2003, BC03) models with exponentially-declining star formation histories, dust attenuation, and a Salpeter IMF to the photometry; details of the grid can be found in N12. Finally, we use `InterRest` (Taylor et al. 2009) to interpolate to rest-frame colors in the Bessell (1990) UBV and 2MASS J filters.

2.3. *HST Grism Spectroscopy*

A total of 14 orbits, split among 3 visits, was devoted to spectroscopy using the G102 and G141 grisms. The spacecraft orientations were spaced by 26 deg and 72 deg from the initial visit to facilitate the deblending of spectral traces. At the beginning of each sequence of grism exposures, a short undispersed exposure through the F160W (for G141) or F105W (for G102) filter was taken to register the grism images, which were then taken following the same dither pattern used for the imaging. The total integration time was 17.0 ks for each grism. In 3 exposures we noticed a rapidly increasing background in the final few reads; we successfully recovered data with the normal background level by masking the final reads and reprocessing the up-the-ramp readouts using `calwfc3`. G102 covers the wavelength range $\simeq 850 - 1140$ nm with a dispersion of 2.4 nm per pixel, whereas G141 spans $\simeq 1110 - 1670$ nm at 4.6 nm per pixel. The wide wavelength range provided by the combination of grisms proved essential to locating the Balmer/4000 Å continuum break at the redshift of JKCS 041.

The grism data were reduced using the `aXe` package (Kümmel et al. 2009). For each object in the catalogs described in Section 2.2 and for each visit, `aXe` generates a calibrated two-dimensional (2D) spectrum and an extracted spectrum, along with estimates of the noise and the flux contamination from other objects. A vertical extraction was used, with the wavelength constant perpendicular to the grism trace. Contamination from overlapping spectra was taken into account using the Gaussian emission model, which estimates the spectrum of each object by linearly interpolating the fluxes in the i, z, F105W, J, and F160W filters and distributes the flux spatially according to the Gaussian shape parameters estimated by `SExtractor`. We found the extracted spectra generated by `aXe` sufficient for deriving emission line redshifts (Section 3.1); however, we made several improvements to the extraction of the brighter sources whose continuum emission we have modeled (Section 3.2).

First, the global background subtraction performed by `aXe` often left significant residual trends, especially for the G102 grism. We improved upon this by fitting and subtracting a linear trend in wavelength to the background pixels in each 2D spectrum, omitting pixels in the extraction aperture and those with significant contaminating flux from other objects. The 2D spectra were created with larger dimensions than the `aXe` default in order to ensure they contain a significant number of blank pixels. With this improvement, the G102 and G141 spectra generally join together smoothly.

Second, `aXe` relies on a Gaussian approximation to the object light profile when it performs optimally-weighted extraction of spectra. While adequate for many objects, this is a poor representation of the extended light profiles of large spheroidal galaxies, which include many of our primary targets. Thus, for each galaxy for which we extract a continuum spectrum, we use the F160W image to measure the light profile in the cross-dispersion direction appropriate to each visit. This profile was then used to extract a 1D spectrum, including error and contamination estimates, from the 2D spectrum with improved weighting. At the same time we measure the light profile of each galaxy in the dispersion direction. In grism spectroscopy this sets the *line spread function* (the LSF, i.e., the spectral resolution) and so is essential for the

modeling we perform in Section 3.2.

3. REDSHIFT MEASUREMENTS AND SPECTRAL FITTING

The WFC3 G102 and G141 grisms represent a powerful combination, particularly for faint continuum spectroscopy: they cover a wide wavelength range continuously with uniform sensitivity, reach magnitudes that remain difficult from the ground, and sample all objects in the field of view with no pre-selection of targets. In this section we describe the measurement of 98 redshifts in the field of JKCS 041, which form the basis for our identification of the cluster members and the study of their properties in the remainder of the paper. The full catalog of redshift measurements is tablulated in Appendix A. Our single WFC3 pointing covers the region within 1 arcmin, or 0.51 Mpc, of the X-ray centroid of JKCS 041. This is well-matched to the virial radius $R_{500} = 0.52$ Mpc estimated by Andreon et al. (2009) based on the X-ray temperature.

The galaxies included in our redshift survey consists of two distinct samples with very different selection properties: an *emission line sample* of galaxies showing one or more spectral lines, and a *continuum sample* of brighter galaxies for which we extract and model the continuum emission. The former is approximately limited by line flux, whereas the latter is limited by broadband flux. In Section 4.4 we estimate how these selections correspond to physical galaxy properties at the cluster redshift.

3.1. *The Emission Line Sample*

We searched for emission lines in the 1D and 2D spectra of all galaxies having $H_{160} < 25.5$ using the plots generated by `aXe2web`. These include contamination estimates, which are very useful for distinguishing true emission lines from overlapping zero order images of other galaxies. We additionally verified the reality of the emission lines by comparing the three independent spectra obtained for each object at the various orientations. In total we identified 63 emission line sources. An example spectrum is shown in the left panel of Figure 1.

Wavelengths of emission lines were measured by fitting Gaussian profiles in `IRAF`. We averaged the wavelengths that were measured separately in each valid spectrum (i.e., each orientation at which the spectrum fell in the field of view and was not strongly contaminated). In 35 of 63 sources unambiguous redshifts were derived through the identification of multiple lines, primarily Hα, [O II], and [O III]. When only a single line was identified (28 sources), it was interpreted as Hα (22 sources) or [O III] (6 sources) depending on which was more consistent with the photometric redshift.

The rms redshift uncertainty was estimated internally from the scatter in independent measurements as $\sigma_z = 0.003$. For 9 galaxies we can compare with redshifts measured at higher spectral resolution in the VIMOS VLT Deep Survey (Le Fèvre et al. 2004). After excluding one outlier with $\Delta z = 0.07$, the rms scatter is $\sigma_{\Delta z} = 0.005$ with no detectable systematic bias. This is 20 times smaller than the median uncertainty in the photometric redshifts of the these galaxies.

We estimate a typical 5σ line flux limit of 5×10^{-17} erg cm^{-2} s^{-1} in G141 data over $\lambda \approx 1.2-1.6\mu$m and in G102 over $\lambda \approx 0.9 - 1.1\mu$m. By simulating artificial emission lines in the extracted spectra, we verified that we would visually identify $\sim 80\%$ of lines exceeding this flux limit. This limit applies to the spectra from each visit, which are the basis of our line search. These have 2–3 orbit depth, which is comparable to the 3D-HST (Brammer et al. 2012) and WISP (Atek et al. 2010) surveys, and these programs have estimated similar limits.

3.2. *The Continuum Sample*

For all galaxies in the *HST* field of view brighter than $H_{160} < 23.3$ with photometric redshifts $1.4 < z_{\rm phot} < 3$, we model the continuum emission in order to derive precise redshifts and stellar population properties. This flux limit corresponds to a typical signal-to-noise ratio of 5 per spectral pixel in the coadded spectra, suitable for continuum fitting, while the redshift range restricts the sample to galaxies for which the Balmer/4000 Å break is expected to fall well within the grism spectral coverage.

For each galaxy, we visually examined the spectra obtained during each of the 3 visits extracted using the improved weighting described in Section 2.3. The contamination model was subtracted from each spectrum. Heavily contaminated wavelength regions, often comprising an entire visit, were identified and masked. The spectra were then coadded using inverse variance weighting to produce a combined spectrum for each grism. The galaxy light profiles, measured for each visit along the dispersion direction (Section 2.3), were averaged with the same weights to estimate the LSF. The exposure times of the spectra vary significantly, since the number of visits that contribute to the stack ranges from 1 to 3. Of the 59 galaxies in the continuum sample, we were able to extract G102 and G141 spectra for 40 objects (68%). The remaining 19 sources were either heavily contaminated by neighboring sources or dispersed off the detector.

To make optimal use of the extensive data we gathered for JKCS 041, we developed a code designed to fit stellar population models jointly to spectroscopic and photometric data with flexible models and arbitrary LSFs. `pyspecfit` is written in Python. It is Bayesian in nature and uses `MultiNest` (Feroz et al. 2009), a Markov Chain Monte Carlo (MCMC) engine, to explore the parameter space and properly estimate uncertainties and degeneracies. The details of the code are described in Appendix B. An example fit is shown in the right panel of Figure 1 for a luminous red galaxy at $z = 2.414$. While our fits are based on the BC03 models, we note in passing that we experimented with using the 2007 models instead, but decided against this due to their uniformly poorer fits to the spectrophotometry. The poorer fits arise from excess light in the rest-frame near-infrared, which is consistent with other studies indicating that the contribution of the TP-AGB stars in these more recent models is overstated (e.g., Kriek et al. 2010; Zibetti et al. 2013).

Only 5 galaxies in the continuum sample show strong emission features; in these cases, we adopt the emission redshift. We slightly increased the noise estimates for the spectral data by 20% to obtain a median $\chi^2_{\rm spec}/n_{\rm pixels} = 1.0$, while for the photometry we find a median $\chi^2_{\rm phot}/n_{\rm filters} = 1.1$. This indicates that the models provide good fits and that the noise estimates are reasonable. The median random uncertainty in $z_{\rm grism}$ is $\sigma_{z_{\rm grism}}/(1+z) = 0.0025$ for the continuum-selected galaxies, which is a factor 15 improvement over their photo-

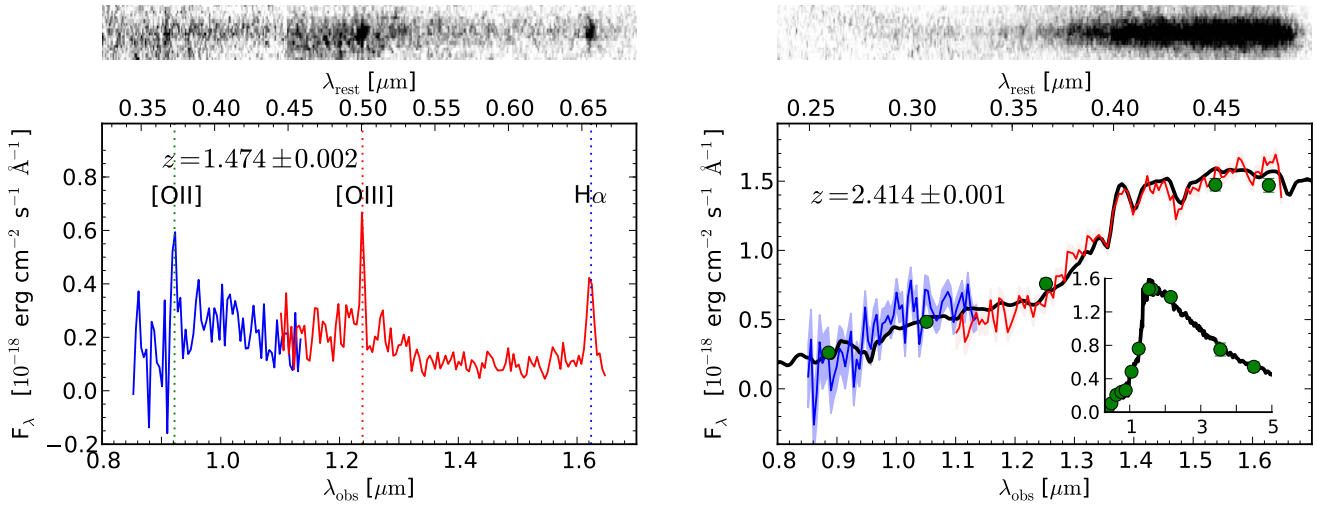

FIG. 1.— **Left:** Example spectrum in which 3 emission lines are identified to yield an unambiguous redshift. **Right:** Example of a luminous ($H_{160} = 21.2$) continuum-selected galaxy at $z = 2.414$ showing a prominent continuum break and several absorption lines. Blue and red lines show the coadded G102 and G141 spectra, respectively, binned to 48 Å pixels with associated 1σ errors shaded. The black line shows the best-fitting model (Section 3.2), and broadband photometry is shown in green. The inset shows the full set of photometry on an expanded wavelength scale. The upper panels show the 2D spectra, displayed without applying a flux calibration.

metric redshift errors.

4. SPECTROSCOPIC CONFIRMATION OF JKCS 041 AND IDENTIFICATION OF MEMBER GALAXIES

The redshift distribution of the emission line and continuum samples is shown in Figure 2. JKCS 041 clearly stands out as a strong overdensity at $z = 1.80$ thanks to the excellent precision of the grism redshifts, which are typically $\sim 15 - 20$ times more precise than the photometric estimates. In this section we isolate a sample of spectroscopically-confirmed member galaxies and discuss their color distribution and star formation activity. We then turn to the alignment of the galaxies with the X-ray emission from the intracluster medium (ICM), before considering the likely completeness of our spectroscopic sample and its relation to a red sequence-based selection.

4.1. *Spectroscopically-confirmed Cluster Members*

The identification of cluster members is relatively unambiguous due to the high precision of the grism redshifts. We selected as cluster members those galaxies for which $> 50\%$ of the integrated probability density $P(z)$ is located within $z_{\rm clus} \pm 3\sigma_z$. Here $P(z)$ is derived from the MCMC chains for the continuum sample and is approximated as a Gaussian for the emission line sample (Section 3.1). We estimate the cluster velocity dispersion $\sigma_v = c\sigma_z/(1+z) = 800$ km s^{-1} based on the X-ray luminosity presented by Andreon et al. (2009) and the scaling relation derived by Zhang et al. (2011) for nearby clusters, which is consistent with with $z \sim 1$ relation determined by Andreon et al. (2008). We began with an initial estimate of $z_{\rm clus}$ and iterate by updating $z_{\rm clus}$ with the mean redshifts of the selected members.

This procedure converged in only one iteration to yield 19 members with a mean redshift of $z_{\rm clus} = 1.803 \pm 0.003$. The selected members are precisely those in the interval $z_{\rm grism} = 1.803 \pm 0.022$, which is indicated by the vertical lines in the lower panel of Figure 2. We note that adopting the velocity window of $\pm 2000(1+z_{\rm clus})$ km s^{-1} advocated by Eisenhardt et al. (2008) would remove only

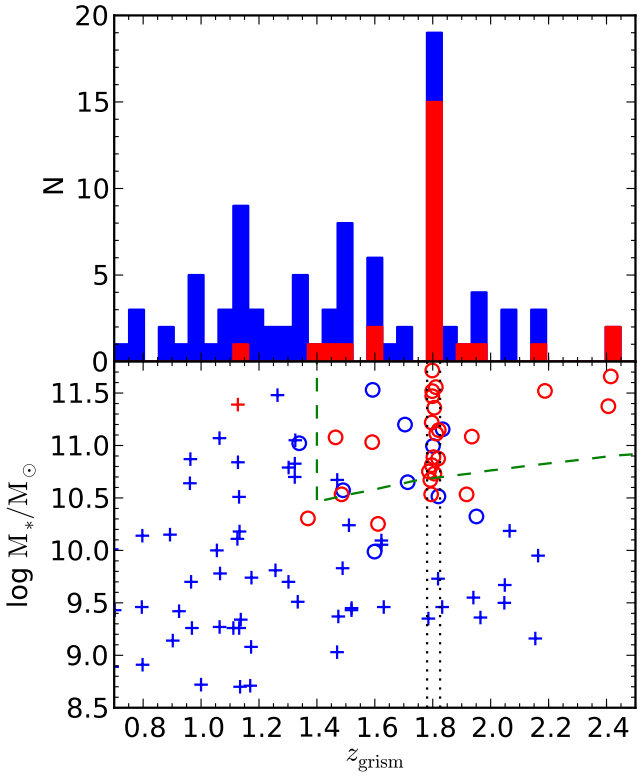

FIG. 2.— **Top:** Distribution of grism redshifts at $z_{\rm grism} > 0.7$ derived from emission lines and continuum fitting. JKCS 041 is the clear spike at $z = 1.8$. Red and blue colors refer to the UVJ-based quiescent and star-forming classifications, respectively (see Figure 4). **Bottom:** Stellar mass and redshift distribution for the same galaxies as in the top panel. Circles and crosses denote continuum and emission line redshifts, respectively. Vertical lines encompass the 19 identified cluster members. The green dashed line approximates the mass completeness of the continuum sample ($z_{\rm phot} > 1.4$, $H_{160} < 23.3$) for a solar metallicity galaxy formed in a burst at $z_f = 5$.

one galaxy from this sample. Among the several previously published estimates of the redshift of JKCS 041, the EAZY photometric redshifts with no corrections applied gave the true $z_{\rm clus}$ (Raichoor & Andreon 2012). Spectra, images, and $P(z)$ distributions for the 19 confirmed members are shown in Figure 3, and their coordinates and photometric properties are listed in Table 1.

Figure 4 shows the distribution of these confirmed cluster members in the UVJ color–color diagram. This plane is frequently used to distinguish quiescent and star-forming systems (Williams et al. 2009), and for the remainder of the paper we refer to quiescent and star-forming galaxies based on this criterion, using the specific form proposed by Whitaker et al. (2011).

Of the 19 confirmed members, 17 arise from the continuum sample, and 15 of of these fall in the quiescent region of the UVJ plane. This large number of confirmed quiescent members makes JKCS 041 an invaluable laboratory for studying environmental processes at high redshifts. None of the quiescent members shows unambiguous ($> 3\sigma$) residual line emission above the continuum models, although there is a hint of [O II] in IDs 657 and 447; the latter galaxy falls near the edge of the quiescent selection box and is the bluest of the quiescent members. Of the star-forming members, 2 show emission lines (IDs 531 and 332) and have low stellar stellar masses $M_* = 10^{9.4-9.8}\,{\rm M}_\odot$, while 2 more massive examples having $M_* = 10^{10.5-11}\,{\rm M}_\odot$ were identified through continuum fitting (IDs 387 and 693). Note that we are able to secure redshifts of these bright blue galaxies even though they lack detectable emission lines.

Morphologically, virtually all of the quiescent confirmed members appear spheroid-dominated (see Figure 3). This visual impression in confirmed by a quantitative analysis of the galaxy shapes in Section 6. Of the 4 star-forming members, 2 appear compact (IDs 693 and 531), ID 332 appears diffuse and irregular, and ID 387 (located near the cluster center) appears to be an inclined disk with a red bulge.

Only one spectroscopic cluster member is detected as an X-ray point source in the 75 ks *Chandra* data (Andreon et al. 2009): ID 352, a UVJ-quiescent galaxy with $L_{X,0.5-2\ {\rm keV}} = 6\times10^{42}$ erg s^{-1}. To investigate the presence of obscured star formation or AGN activity in other sources, we measured 24μm fluxes in the *Spitzer* Multiband Imaging Photometer (MIPS) data taken for the SWIRE survey.[6] None of the quiescent members is detected at 2σ significance (> 0.13 mJy), and there is no detection in a mean stack to a 2σ limit of 16 μJy. The 2 more massive star-forming members (IDs 387 and 693) are detected with fluxes of 0.20 ± 0.06 mJy each. Based on the Wuyts et al. (2008) templates, this corresponds to a total infrared luminosity of $L_{\rm IR} = (1.3\pm0.4)\times10^{12} L_\odot$ for each source and SFRs of $140 \pm 44\ M_\odot\ {\rm yr}^{-1}$ for a Chabrier (2003) IMF (Bell et al. 2005). These are typical for star-forming galaxies in this mass and redshift range (e.g., Reddy et al. 2006).

4.2. *Alignment with X-ray emission*

[6] We used a simple 7″ diameter aperture and applied an aperture correction factor of 2.56. The X-ray source (ID 352) has a detected close neighbor whose flux was subtracted using a PSF model.

Figure 5 shows that the distribution of confirmed cluster members is clearly centered upon the diffuse X-ray emission discovered by Andreon et al. (2009). Their centroid of R.A. = 02:26:44.0 ± 6 arcsec, Dec. = –04:41:36 ± 4 arcsec (red box in Figure 5) coincides with the X-ray centroid determined by Andreon et al. within the small 1σ uncertainties. The cluster members are not distributed uniformly over the field; all lie within R_{500} of the X-ray center, and the majority are confined to a much smaller, elongated structure overlapping the X-ray emission. Together with the large number of massive, red galaxies we have confirmed as cluster members, we consider this clear evidence that the X-ray emission originates from the ICM of JKCS 041. After making a small correction to the luminosity distance, the bolometric X-ray luminosity estimated by Andreon et al. (2009) is $(6.5\pm1.5)\times10^{44}$ erg s^{-1} within R_{500}.

The two strongest peaks in the redshift distribution other than at the cluster are at $z = 1.48$ and 1.13. In Figure 6 we show the locations of the galaxies in these structures relative to JKCS 041 and the X-ray emission. The $z = 1.48$ structure appears to be a group composed mostly of lower-mass blue galaxies; the total stellar mass associated with this system is $\sim 14\times$ lower than JKCS 041. Thus, it is not likely to be the source of the vast majority of the X-ray emission. The second peak is visible in the grism emission line sample at $z = 1.13$, but it also contains red galaxies whose redshifts are too low to be included in our continuum sample. We therefore plot a more complete sample of 7 galaxies having $M_* > 10^{11}\,{\rm M}_\odot$ and $z = 1.13\pm0.1$, where the photometric redshift is applied to sources without a spectroscopic measurement. As shown by Andreon & Huertas-Company (2011), the galaxies in this structure are offset by 1 arcmin southeast of the X-ray emission. Although Bielby et al. (2010) located this structure and considered it a possible source of the X-ray emission, they were unable to locate JKCS 041 spectroscopically in a ground-based optical redshift survey. With the less biased selection and dense sampling afford by the WFC3 grisms, we are able to show convincingly that the X-ray emission originates from the $z = 1.80$ cluster.

4.3. *The Red Sequence*

In the absence of spectroscopic data, members of high-redshift clusters are frequently identified based on the red sequence. With our grism observations we can assess the purity and completeness of this method. Figure 7 shows the color–magnitude diagram for galaxies with $R < R_{500}$, where R is the distance from the X-ray centroid.

JKCS 041 shows a clear red sequence with a mean observed color $\langle z-J\rangle = 1.98\pm0.02$ and a measured scatter of $\sigma_{z-J} = 0.07$. This is comparable to the rms measurement error of $\delta_{z-J} = 0.09$, indicating that the intrinsic scatter is low (Andreon 2011). We define red sequence galaxies as those within $\pm2\sigma$ of the mean color to a limiting magnitude of $H_{160} < 23.3$ (dashed in Figure 7).

The majority of the spectroscopically confirmed members in the flux-limited continuum sample (13 of 17) are on the red sequence. However, in addition to the 2 star-forming members, 2 galaxies that are classified as quiescent according to their UVJ colors are bluer than the $z-J$ red sequence (IDs 255 and 447). These are likely among the most recently truncated systems. Naturally,

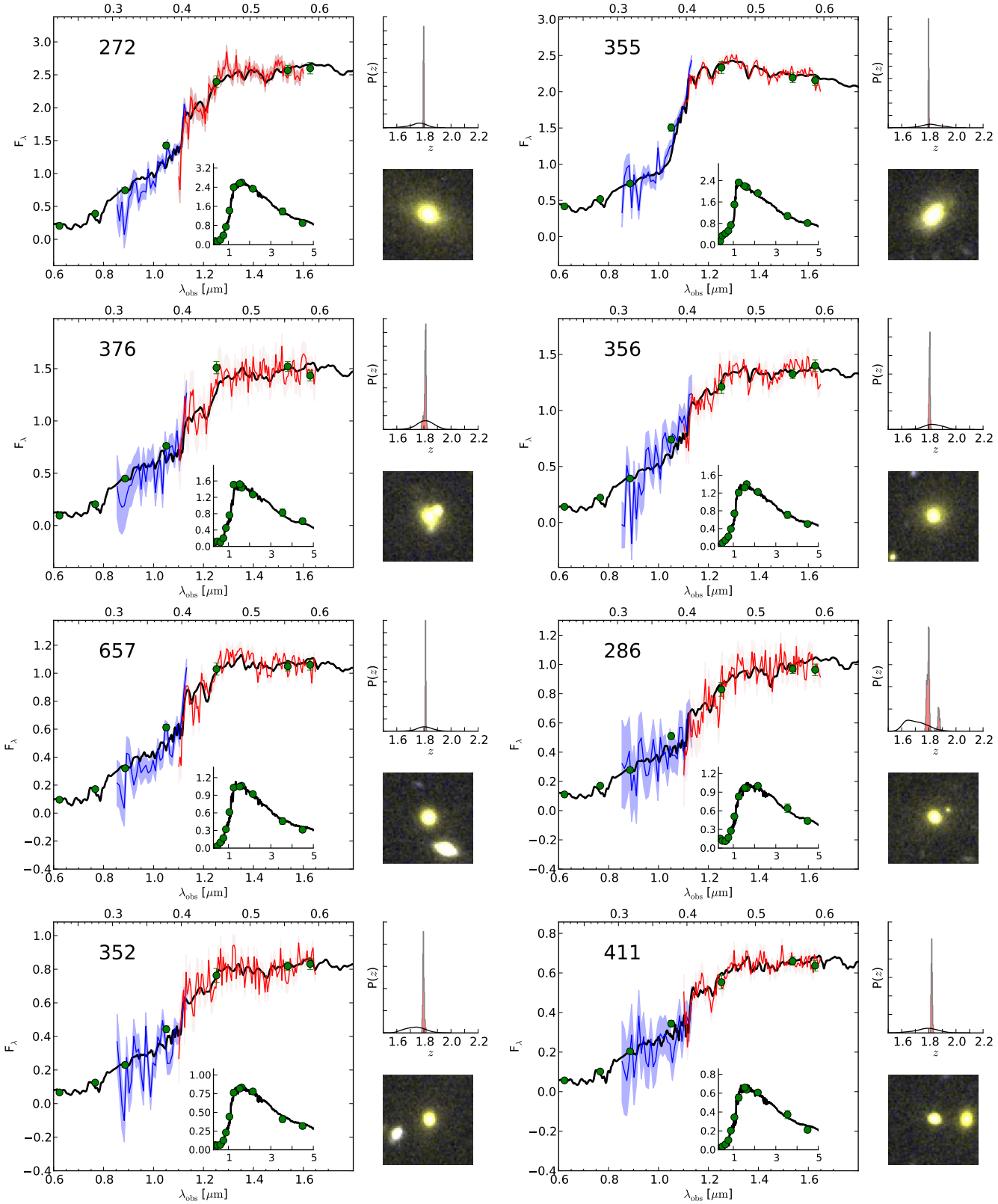

FIG. 3.— Spectroscopically confirmed cluster members. For each object, the main panel shows the grism spectra (blue is G102, red is G141, 1σ errors are shaded) binned to 48 Å (red) and 96 Å (blue) pixels for display purposes. Photometry (green circles) and the best-fitting model (black) are overlaid. The top and bottom axes shows the rest- and observed-frame wavelength in nm, and the units of F_λ are 10^{-18} erg cm^{-2} s^{-1} Å^{-1}. The inset shows the complete photometry on an expanded scale in the same units. Cutouts show F105W/F160W images, displayed on a linear scale, with a side length of $5''$. The $P(z)$ subpanels show the redshift probability density derived from the broadband photometry only using `EAZY` (black curves) and from our joint fits to the spectra and photometry (filled histograms). Galaxies are ordered by decreasing F160W flux. For the two galaxies in the emission line sample (IDs 332 and 531) no continuum fit is plotted.

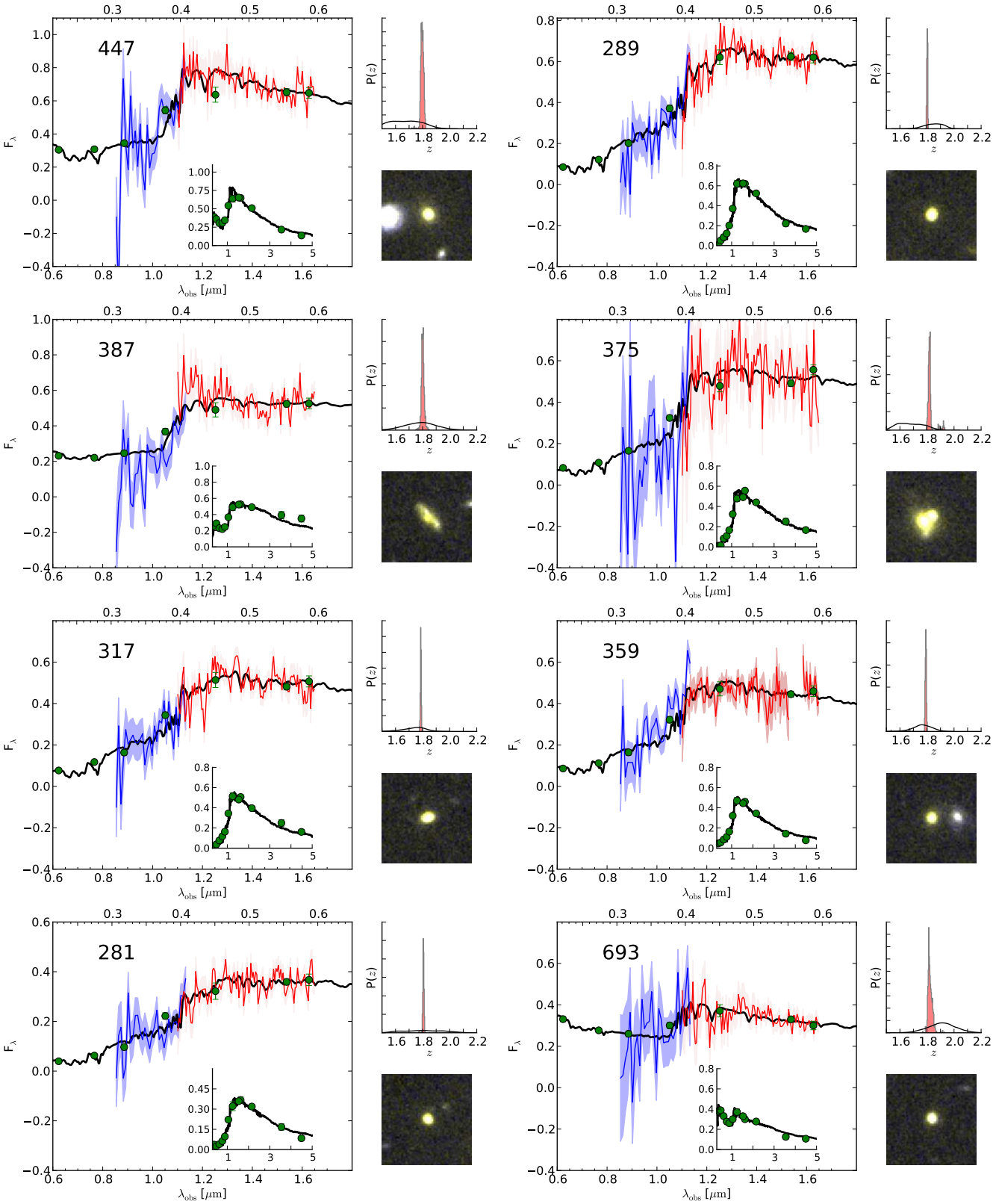

FIG. 3.— Continued

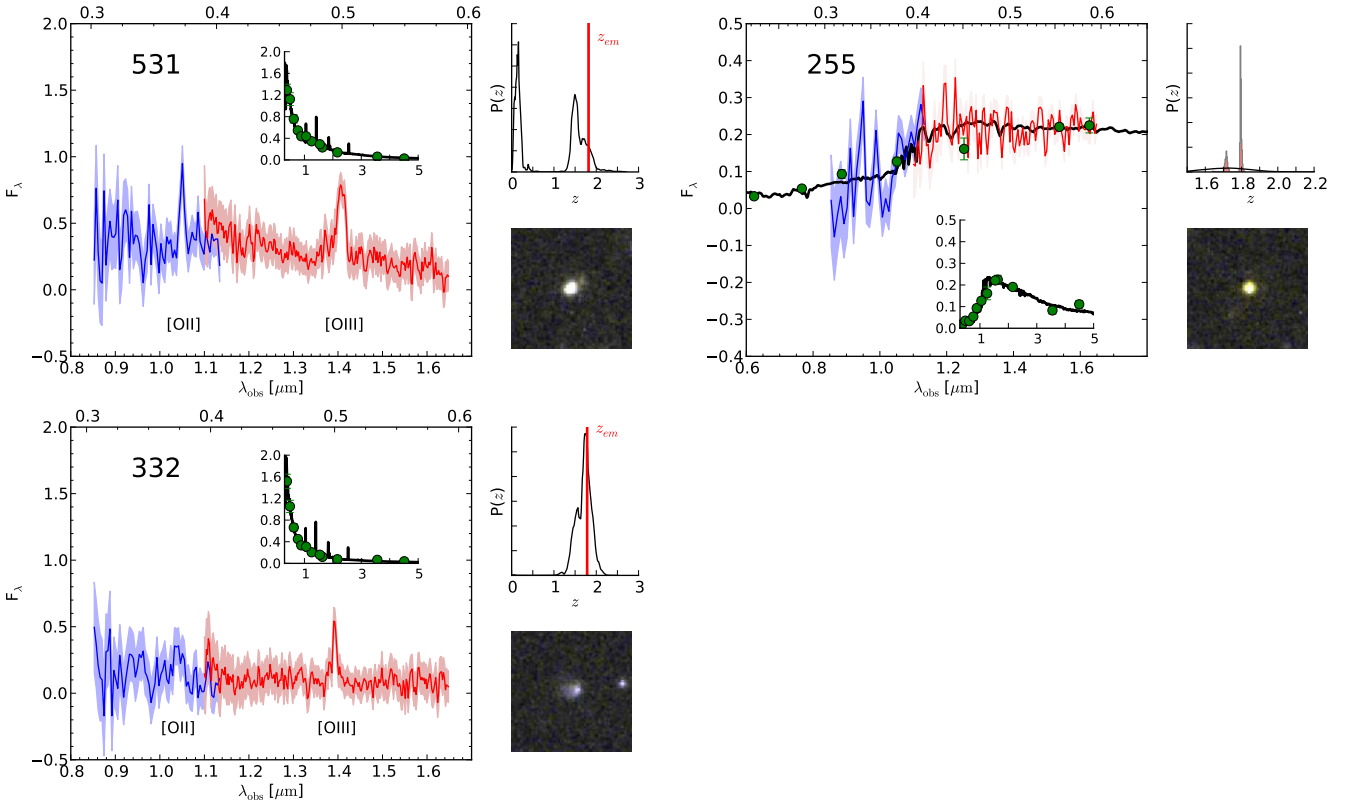

FIG. 3.— Continued

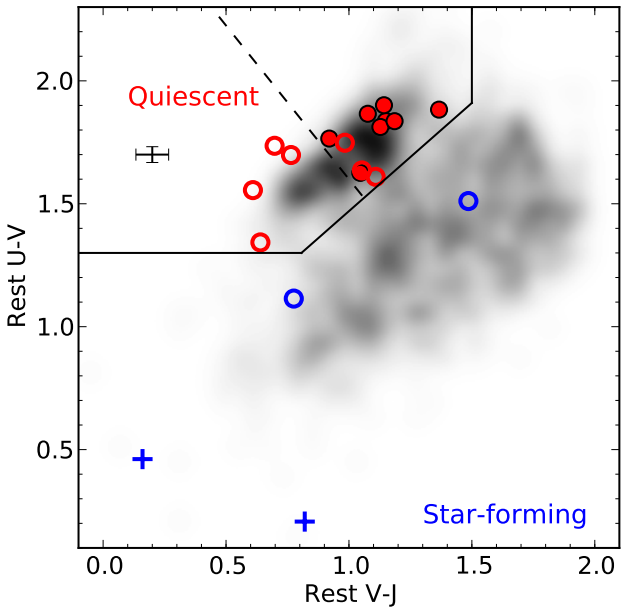

FIG. 4.— Colors of the spectroscopically-confirmed cluster members. Circles and crosses denote galaxies with continuum and emission line redshifts, respectively, while filled and open symbols denote massive ($M_* > 10^{11}\,M_\odot$) and less massive ($M_* < 10^{11}\,M_\odot$) systems, respectively. The greyscale shows the field distribution for galaxies drawn from the NMBS survey (see Section 5.1) that have $z = 1.8 \pm 0.2$ and $M_* > 10^{10.6}\,M_\odot$. The solid line divides the quiescent and star-forming selection regions, while the dashed line shows the partition between bluer and redder quiescent galaxies used by Whitaker et al. (2013). Median color uncertainties are illustrated by the error bar.

some galaxies located on the $z - J$ red sequence will not be associated with the cluster. Using the grism redshifts, we identified 5 interlopers over the full field of view, which are indicated by boxes in Figure 5. Only 2 of these are located at $R < R_{500}$. Thus, a red sequence selection yields a fairly pure and complete sample (13 of 15, or 87%) of quiescent members within $R < R_{500}$, as anticipated from the high overdensity of red sequence galaxies compared to the field (Andreon & Huertas-Company 2011). At larger radii contamination is more severe.

4.4. *Completeness*

While our continuum-selected sample is strictly flux-limited, it is nearly mass-limited at fixed redshift: based on the catalog of N12 that covers a much wider area, we expect 88% of galaxies at $z = 1.8$ with $M_* > 10^{10.6}\,M_\odot$ to be brighter than $H_{160} = 23.3$. Independently, we estimate nearly the same limiting mass using the BC03 model for a solar-metallicity galaxy formed in a burst at $z_f = 5$ (see green line in Figure 2, lower panel). Conversely, all confirmed members in the continuum sample have $M_* > 10^{10.5}\,M_\odot$. For the emission line sample, the limiting line fluxes derived in Section 3.1 correspond to line luminosities of $3 \times 10^8 L_\odot$ at the redshift of JKCS 041. In [O II] emission this corresponds to a limiting SFR of 30 $M_\odot\,\mathrm{yr}^{-1}$ according to the Kewley et al. (2004) calibration with dust attenuation of $A_V = 1$. For galaxies with significantly subsolar metallicity, the [O II] emission will be weaker, but [O III] will be more visible. The signal-to-noise in grism spectroscopy also depends on morphology, and limits for very extended objects will be weaker.

Thus, with the caveats mentioned above, the parent spectroscopic sample should be reasonably complete for

TABLE 1
Redshifts and photometric data for spectroscopically confirmed cluster members and red sequence members

ID	R.A.	Dec.	H_{160}	z	Type	$\log M_*^{\rm auto}/{\rm M}_\odot$	$z-J$	$(U-B)_{\rm r}$	$(U-V)_{\rm r}$	$(V-J)_{\rm r}$	UVJ class
Spectroscopically confirmed cluster members											
272	36.68173	-4.68934	20.63	$1.798^{+0.002}_{-0.003}$	C	11.71 ± 0.03	2.02 ± 0.04	1.20	1.84	1.15	Q
355	36.68644	-4.69239	20.80	$1.798^{+0.002}_{-0.002}$	C	11.52 ± 0.02	2.01 ± 0.03	1.15	1.63	1.05	Q
376	36.67501	-4.69286	21.20	$1.811^{+0.004}_{-0.008}$	C	11.56 ± 0.03	2.07 ± 0.05	1.34	1.90	1.14	Q
356	36.69423	-4.69235	21.35	$1.805^{+0.003}_{-0.004}$	C	11.36 ± 0.04	1.97 ± 0.07	1.16	1.81	1.13	Q
657	36.67557	-4.70257	21.61	$1.812^{+0.002}_{-0.002}$	C	11.11 ± 0.02	2.02 ± 0.05	1.20	1.77	0.92	Q
286	36.68790	-4.68994	21.69	$1.798^{+0.068}_{-0.013}$	C	11.47 ± 0.03	1.94 ± 0.08	1.16	1.88	1.37	Q
352	36.69051	-4.69215	21.88	$1.797^{+0.006}_{-0.004}$	C	11.22 ± 0.05	2.05 ± 0.08	1.23	1.87	1.08	Q
411	36.67382	-4.69384	22.11	$1.821^{+0.004}_{-0.004}$	C	11.15 ± 0.04	1.84 ± 0.09	1.11	1.84	1.19	Q
447	36.69121	-4.69487	22.12	$1.797^{+0.011}_{-0.009}$	C	10.81 ± 0.03	1.42 ± 0.09	0.82	1.34	0.64	Q
289	36.68965	-4.68994	22.17	$1.802^{+0.003}_{-0.004}$	C	10.89 ± 0.03	1.97 ± 0.08	1.18	1.74	0.70	Q
387	36.68231	-4.69296	22.36	$1.801^{+0.009}_{-0.009}$	C	11.00 ± 0.04	1.50 ± 0.11	0.94	1.51	1.49	SF
375	36.67488	-4.69278	22.43	$1.819^{+0.008}_{-0.008}$	C	10.88 ± 0.02	1.91 ± 0.09	1.09	1.64	1.05	Q
317	36.69911	-4.69091	22.45	$1.787^{+0.003}_{-0.003}$	C	10.75 ± 0.04	2.00 ± 0.11	1.14	1.61	1.11	Q
359	36.67696	-4.69228	22.54	$1.792^{+0.004}_{-0.005}$	C	10.67 ± 0.03	1.90 ± 0.11	1.10	1.56	0.61	Q
281	36.69061	-4.68944	22.77	$1.806^{+0.004}_{-0.004}$	C	10.73 ± 0.06	2.06 ± 0.17	1.12	1.75	0.98	Q
693	36.67771	-4.70379	22.86	$1.820^{+0.019}_{-0.010}$	C	10.51 ± 0.05	1.14 ± 0.09	0.75	1.11	0.78	SF
531	36.67919	-4.69839	23.12	$1.818^{+0.002}_{-0.002}$	E	9.73 ± 0.06	0.49 ± 0.11	0.27	0.46	0.16	SF
255	36.68793	-4.68838	23.30	$1.795^{+0.004}_{-0.075}$	C	10.53 ± 0.04	1.35 ± 0.24	0.85	1.70	0.76	Q
332	36.67165	-4.69125	23.83	$1.785^{+0.003}_{-0.003}$	E	9.35 ± 0.28	0.22 ± 0.21	0.11	0.21	0.82	SF
Candidate cluster members on red sequence (not spectroscopically confirmed), $H_{160} < 23.3$ and $R < R_{500}$											
772	36.67527	-4.70738	22.26	$1.81^{+0.08}_{-0.11}$	P	10.91 ± 0.28	2.00 ± 0.09	1.20	1.72	1.00	Q
275	36.68274	-4.68931	22.68	$1.81^{+0.12}_{-0.19}$	P	10.78 ± 0.28	1.87 ± 0.17	1.00	1.66	1.02	Q
404	36.68949	-4.69338	22.89	$1.59^{+0.17}_{-0.09}$	P	10.71 ± 0.28	1.86 ± 0.16	1.22	1.91	1.33	Q

Note. — The "r" subscript denotes colors in the rest frame. C and E types indicate continuum and emission line redshifts, whereas P denotes photometric redshifts. Q and SF refer to galaxies in the quiescent and star-forming regions of the UVJ color–color plane. For type C, M_* is derived from fits to the full spectrophotometry (Section 3.2); for types E and P, M_* is based on `FAST` fits to the photometry. Median random uncertainties in the rest-frame $U-B$, $U-V$, and $V-J$ colors are 0.07, 0.03, and 0.08 mag, respectively. H_{160} is F160W magnitude in the `MAG_AUTO` aperture, and $M_*^{\rm auto}$ is scaled here to this total flux.

stellar masses $M_* > 10^{10.6} M_\odot$ and star-formation rates $\gtrsim 30 M_\odot$ yr^{-1}. Additional incompleteness arises from those spectra that could not be extracted due to contamination from nearby sources. This affects 19 of the 59 galaxies in the continuum sample (Section 3.2). Three of these lie on the red sequence and are located at $R < R_{500}$. These are likely cluster members whose properties we list in Table 1. Three additional bluer systems located within R_{500} have $z_{\rm phot}$ consistent with JKCS 041 within their 68% confidence intervals; however, the redshift uncertainties are too large to associate them with the cluster with any confidence. None of the candidate members discussed above has a stellar mass $M_* > 10^{11}\,{\rm M}_\odot$. Therefore, most likely we have spectroscopically confirmed all members with $M_* > 10^{11}\,{\rm M}_\odot$ and $R < R_{500}$. At lower masses $M_* = 10^{10.6-11}\,{\rm M}_\odot$, considering the 3 most likely photometric candidates, our estimated spectroscopic completeness is $\sim 75\%$. Given this high completeness, for the rest of the paper we focus our analysis on the spectroscopically confirmed cluster members.

5. STELLAR POPULATIONS OF QUIESCENT GALAXIES: JKCS 041 COMPARED TO THE FIELD

Having identified a well-defined set of cluster members based on grism spectroscopy, we now turn to the effect of the cluster environment on their stellar populations. We first consider the fraction of quenched systems in JKCS 041 relative to coeval field galaxies of matched stellar mass. Additional insight can then be gained from the ages of the quiescent cluster members. We construct composite spectra that reveal age-sensitive stellar absorption lines at high signal-to-noise for the first time in such a distant cluster. Using these, we investigate the mean stellar age both as a function of mass within the cluster, and relative to similar field galaxies whose composite spectrum was constructed by Whitaker et al. (2013) using 3D-HST grism data. The 17 spectroscopically-confirmed cluster members in the continuum sample, which is nearly mass-limited (Section 4.4), form the basis for the following comparisons.

5.1. *The Quiescent Fraction*

Figure 8 compares the fraction f_Q of galaxies in JKCS 041 with quiescent UVJ colors to that of field galaxies in the same range of stellar mass and redshift. The comparison sample is drawn from the NEWFIRM Medium Band Survey catalogs in the AEGIS and COSMOS fields (Whitaker et al. 2011), selected from $z_{\rm phot} = 1.8 \pm 0.2$ and converted to a Salpeter IMF. Although this "field" sample includes galaxies that inhabit a range of environments, a differential comparison is still

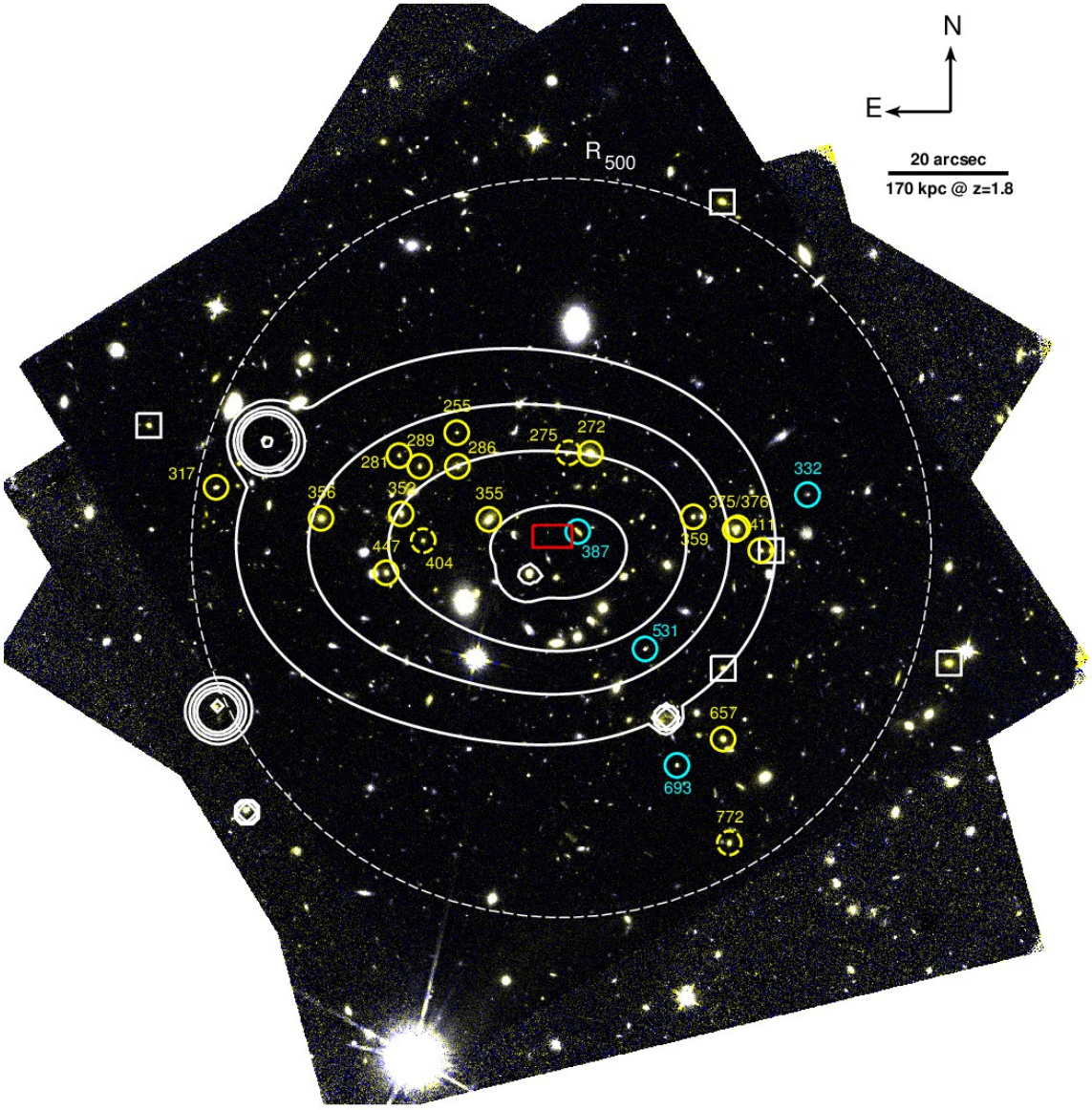

FIG. 5.— *HST*/WFC3 image of JKCS 041 in the F160W and F105W filters. Confirmed cluster members are indicated by yellow (quiescent galaxies) and light blue (star-forming) circles. The smoothed *Chandra* X-ray emission (Andreon et al. 2009) is overlaid as contours. The centroid of the confirmed members and its 1σ uncertainty is shown by the red rectangle, which is well-aligned with the X-ray centroid. Dashed circles show the candidate cluster members on the red sequence with contaminated spectra that preclude a spectroscopic determination; white squares show spectroscopically confirmed non-members that are on the cluster red sequence (Section 4.4).

informative because JKCS 041 is a strong overdensity.[7]

Clearly, the cluster environment has had a powerful role in determining the number of quenched systems: 88% (15 of 17) of the cluster members in the continuum sample are quiescent, whereas this fraction is less than half in the field. Roughly half of the quiescent cluster members were thus quenched by cluster-related processes. Recalling that our spectroscopic sample may be missing some cluster members with masses $M_* = 10^{10.6-11}\,\mathrm{M}_\odot$ due to contamination of their spectra, we have tested the effects of adding in the 6 unconfirmed candidate members described in Section 4.3. This would move f_Q in the lowest-mass bin only with the plotted 1σ uncertainty, resulting in a fraction that would still be elevated above the field. Using a photometric redshift selection and a statistical background subtraction, Raichoor & Andreon (2012) also estimated a high quiescent fraction $f_Q \gtrsim 85\%$ (1σ limit) among massive galaxies ($M_* \gtrsim 10^{11}\,\mathrm{M}_\odot$) in the core of JKCS 041 ($R < 0.5R_{200}$), consistent with our spectroscopic sample.

[7] For example, 9 members having $M_* > 10^{11}\,\mathrm{M}_\odot$ lie within 1 arcmin of the cluster center, whereas only 1.8 are expected from the mean surface density in the field.

5.2. *Composite Spectra of Quiescent Cluster Members*

Having determined that the efficiency of quenching in JKCS 041 is high, we now consider the ages of its quiescent members by constructing composite spectra of these galaxies. Stacking increases the signal-to-noise ratio and averages over residual contamination or back-

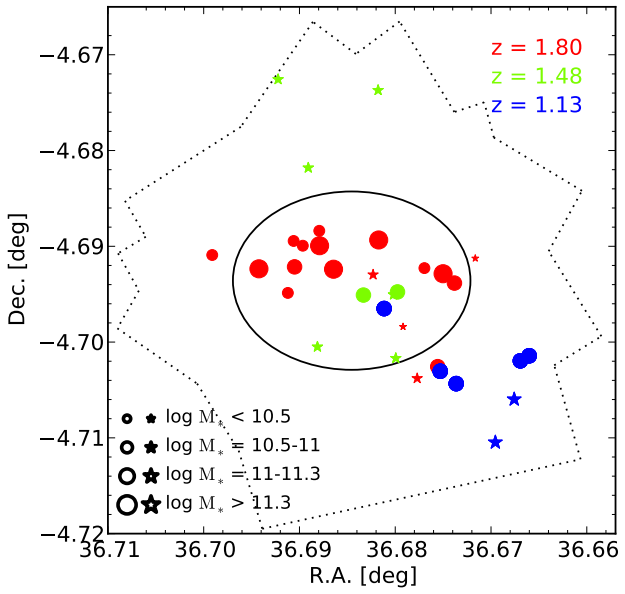

FIG. 6.— Peaks of the redshift distribution in the field of JKCS 041. Spectroscopic members of JKCS 041 are indicated by red symbols, whose positions trace the X-ray emission marked by the solid ellipse (outer contour from Figure 5). Also shown in green and blue are are two foreground structures at $z_{\rm grism} = 1.48 \pm 0.02$ and $z_{\rm phot} = 1.13 \pm 0.1$, respectively, which we conclude are unlikely to be associated with the X-ray emission. Stars and circles distinguish star-forming and quiescent galaxies of various stellar masses. The dotted line shows the border of our *HST* imaging.

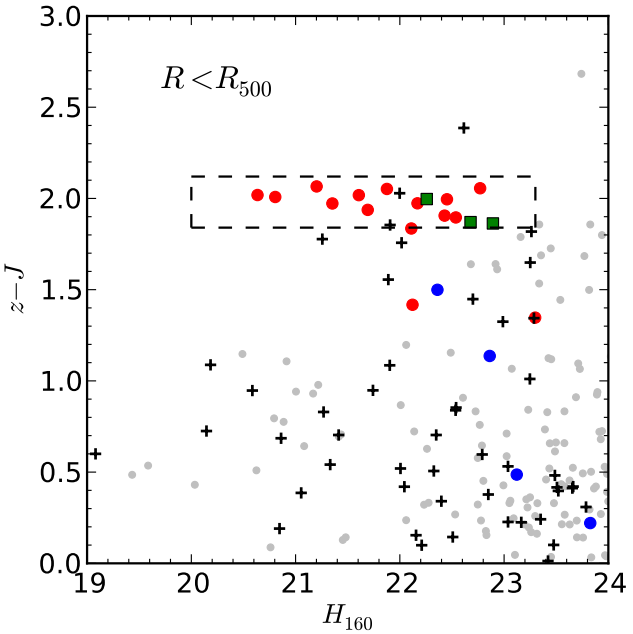

FIG. 7.— The red sequence of JKCS 041. *Red circles:* Spectroscopically-confirmed quiescent cluster members. *Blue circles*: Confirmed star-forming members. *Black crosses:* Confirmed non-members. *Green squares:* Candidate cluster members on the red sequence (dashed region) that lack a grism redshift due to contamination of their spectra. *Gray circles:* Remaining galaxies with no grism redshift. Only galaxies within R_{500} of the cluster center are plotted; this includes all confirmed members.

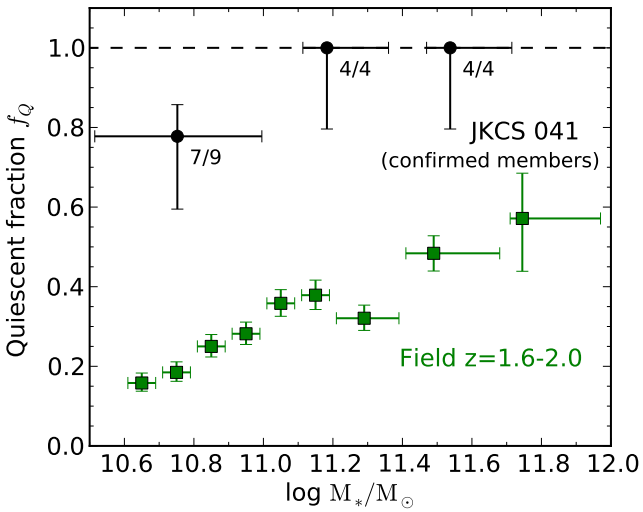

FIG. 8.— Fraction of galaxies classified as quiescent by their UVJ colors in several stellar mass bins. Spectroscopic members of JKCS 041 (black) are compared to coeval field galaxies drawn from the NMBS survey (green). Horizontal error bars show the range of masses in each bin, with points placed at the median mass, while vertical 1σ errors are based on binomial statistics.

ground subtraction errors that may affect individual spectra. Rather than stacking the flux-calibrated spectra and photometry, we average continuum-normalized spectra covering $\simeq 4000 - 5900$ Å redward of continuum break. This technique has several advantages. First, we are able to measure the age-sensitive Balmer (Hβ,γ,δ) and Mg b absorption lines; since these are narrowband features, they are more robust against errors in the continuum shape and uncertainties in dust attenuation. Second, we avoid the rest-frame near-infrared where model uncertainties related to the TP-AGB phase can influence the derived ages around 1 Gyr. Third, we are able to make a homogeneous comparison to coeval, quiescent galaxies in the field, whose composite continuum-normalized spectrum was measured by Whitaker et al. (2013) using 3D-HST survey data.

In order to investigate mass-dependent trends, we split the sample of 15 confirmed quiescent members into a higher-mass subsample consisting of 8 galaxies with $M_* > 10^{11}\,{\rm M}_\odot$, and a lower-mass subsample whose 7 members span $M_* = 10^{10.5-11}\,{\rm M}_\odot$. The continuum of each spectrum was first determined by fitting a third order polynomial to the models shown in Figure 3, excluding the strong absorption lines. Each spectrum was then divided by the continuum, shifted to the mean redshift of the cluster, and interpolated onto a grid with 48 Å pixels (17 Å in the rest frame), which is close to the native dispersion. The spectra were then combined by averaging each spectral pixel, excluding the highest and lowest measures. Uncertainties were estimated by bootstrapping. The LSFs of the galaxies entering the stack (Section 2.3) were also averaged to construct a mean LSF.

We fit the stacked spectra to simple stellar population (single-burst) models using `pyspecfit`, taking the redshift, age, and metallicity as free parameters. The model spectra were continuum-normalized using the same method that was applied to the data. A broad, log-uniform prior was placed on the age. We allow the metallicity to vary to quantify the degeneracy with age.

Since these galaxies are expected to evolve into the cores of present-day massive ellipticals (e.g., Bezanson et al. 2009; Hopkins et al. 2009), which are metal-enriched to [Z/H] $\approx 0.1 - 0.3$ (e.g., Thomas et al. 2010; Conroy et al. 2013), we place a broad uniform prior on [Z/H] over the range 0–0.3.

The top left panel of Figure 9 shows the spectrum of the more massive ($M_* > 10^{11}\,M_\odot$) quiescent members of JKCS 041. The quality of the spectrum is remarkably high, with a signal-to-noise ratio of 55 per pixel, and it clearly shows several absorption lines as indicated in the figure. The model (black curve) fits the data well with an age of $1.45^{+0.24}_{-0.18}$ Gyr, marginalized over metallicity, which corresponds to a formation redshift $z_f = 3.0^{+0.4}_{-0.2}$.

The lower left panel displays the mean spectrum of the lower-mass ($M_* = 10^{10.5-11}\,M_\odot$) quiescent members. Although the spectrum is necessarily noisier, with a signal-to-noise ratio of 22, it is clearly different from that of the higher-mass galaxies. The clearest difference is the enhanced strength of the Balmer absorption lines: Hβ, Hγ, Hδ are all markedly deeper in the lower mass sample. We derive a younger luminosity-weighted mean age of $0.90^{+0.19}_{-0.10}$ Gyr, corresponding to a formation redshift $z_f = 2.4^{+0.2}_{-0.1}$. The Mg b absorption in this spectrum is too deep to be matched even by a maximally-old, metal-rich model; this may be due to residual non-Gaussian noise in the stack. In any case, masking Mg b shifts our age inference by only $\sim 1\sigma$ to 0.79 ± 0.19 Gyr (dashed lines in Figure 9).

The quiescent galaxies in JKCS 041 thus have a range of ages that follow the well-known mass-dependent trends seen in the field, in which lower-mass early-type galaxies typically have younger luminosity-weighted ages (e.g., Treu et al. 2005; Thomas et al. 2010). Although the absolute ages depend somewhat on metallicity, the right panel of Figure 9 shows that the age difference of 0.52 ± 0.26 Gyr between the two subsamples is more robust, provided that they have broadly similar metallicity. We indeed expect the mean metallicities of our mass-selected subsamples to differ by $\lesssim 0.1$ dex, based on abundance studies at low redshift.[8]

Two additional pieces of data support this conclusion. First, the ages of the individual galaxies as measured from fits to their grism spectra and photometry (Section 3.2) show the same trend: the median age is 1.6 Gyr and 0.96 Gyr for the high- and low-mass subsamples, respectively, which is consistent with the ages derived from their mean continuum-normalized spectra. Second, the lower-mass galaxies have bluer colors, as shown in Figure 4. We can predict the mean color differences between the mass-selected subsamples that should arise purely from the difference in ages inferred from their absorption lines. The predicted $\Delta\langle U - V\rangle = 0.14 \pm 0.08$ and $\Delta\langle V - J\rangle = 0.26 \pm 0.12$ are consistent with the measured values of $\Delta\langle U - V\rangle = 0.20$ and $\Delta\langle V - J\rangle = 0.29$. Thus, the color trend can be explained by a mass-dependent trend in age, rather than metallicity or dust content.

These results should be interpreted with the usual understanding the the ages are luminosity-weighted and so skew toward the most recent star-formation episode. Our focus is robustly constraining the mean age as a function of mass, and some cluster members at given mass may of course be older or younger. (For example, the spectrum of ID 355, shown in Figure 3, is clearly younger than that of the first-rank cluster member.) The tightness of the red sequence led Andreon (2011) to infer that the spread in ages at a fixed mass is quite small; this will be analyzed using our spectroscopic data in a subsequent paper (Andreon et al., in preparation).

[8] Given the ratio of the median stellar masses entering our two bins, we estimate a velocity dispersion ratio of $\Delta \log \sigma \approx 0.2$, which corresponds to abundance variations of Δ[Fe/H] ≈ 0.03 and Δ[Mg/Fe] ≈ 0.08 in $z \sim 0$ ellipticals (Conroy et al. 2013).

5.3. *Age and Line Emission in Quiescent Galaxies as a Function of Environment*

Whitaker et al. (2013) recently constructed composite spectra of 171 quiescent field galaxy observed in the 3D-HST grism survey. This presents an interesting opportunity to compare quenched field and clusters galaxies at the same early epoch. The Whitaker et al. data are very well suited for this comparison. In addition to being observed with the same instrument, they selected quiescent galaxies using the same UVJ color selection, and their limiting magnitude of $H_{140} < 22.8$ (measured in the F140W filter) is similar to our limit of $H_{160} < 23.3$. Their median stellar mass $10^{11.08}\,M_\odot$, converted to a Salpeter IMF, matches the $10^{11.11}\,M_\odot$ of our sample. The main difference is that the Whitaker et al. stacks combine field galaxies spanning a wide range in redshift, $z = 1.4 - 2.2$, whereas the members of JKCS 041 are obviously at a single redshift. Nonetheless, the median redshift of the galaxies in their stacks is $\langle z\rangle \simeq 1.6 - 1.7$, close to JKCS 041.

Rather than subdividing their sample by stellar mass, Whitaker et al. split the quiescent selection region of the UVJ plane into two regions indicated by the dashed line in Figure 4. Among the quiescent JKCS 041 members, such a color division is very similar to a division in stellar mass: the 8 quiescent members with $M_* > 10^{11}\,M_\odot$ would all fall in the redder subsample of Whitaker et al., and the 7 less massive members fall in or near their bluer region. The mean color difference between the galaxies in their blue and red subsamples ($\Delta\langle U - V\rangle = 0.2$, $\Delta\langle V - J\rangle = 0.3$) is consistent with that described above for our mass-selected subsamples.

With this in mind, in the top left panel of Figure 9 we compare our composite spectrum of massive JKCS 041 members to the composite field spectrum of redder quiescent galaxies investigated by Whitaker et al. First, we note that the Mg b lines are nearly identical. Correspondingly, Whitaker et al. derived an age of $1.6^{+0.5}_{-0.4}$ Gyr for their redder field sample, consistent with our measurement (see right panel). Interestingly, the field stacks show faint line emission in [O III] $\lambda\lambda 4959, 5007$ and in filling of Hβ, whereas the spectrum of the JKCS 041 members clearly lacks this emission and instead follows the stellar population model closely.

In the lower left panel of Figure 9 we compare our composite spectrum of lower-mass JKCS 041 members to the composite spectrum of bluer quiescent field galaxies. The strong Balmer lines seen in the cluster members are also evident in the field. Whitaker et al. derived a reduced age of $0.9^{+0.2}_{-0.1}$ Gyr, again consistent with our measurement for the lower-mass ($M_* = 10^{10.5-11}\,M_\odot$) quiescent cluster members. Whitaker et al. infer [O III] emission in

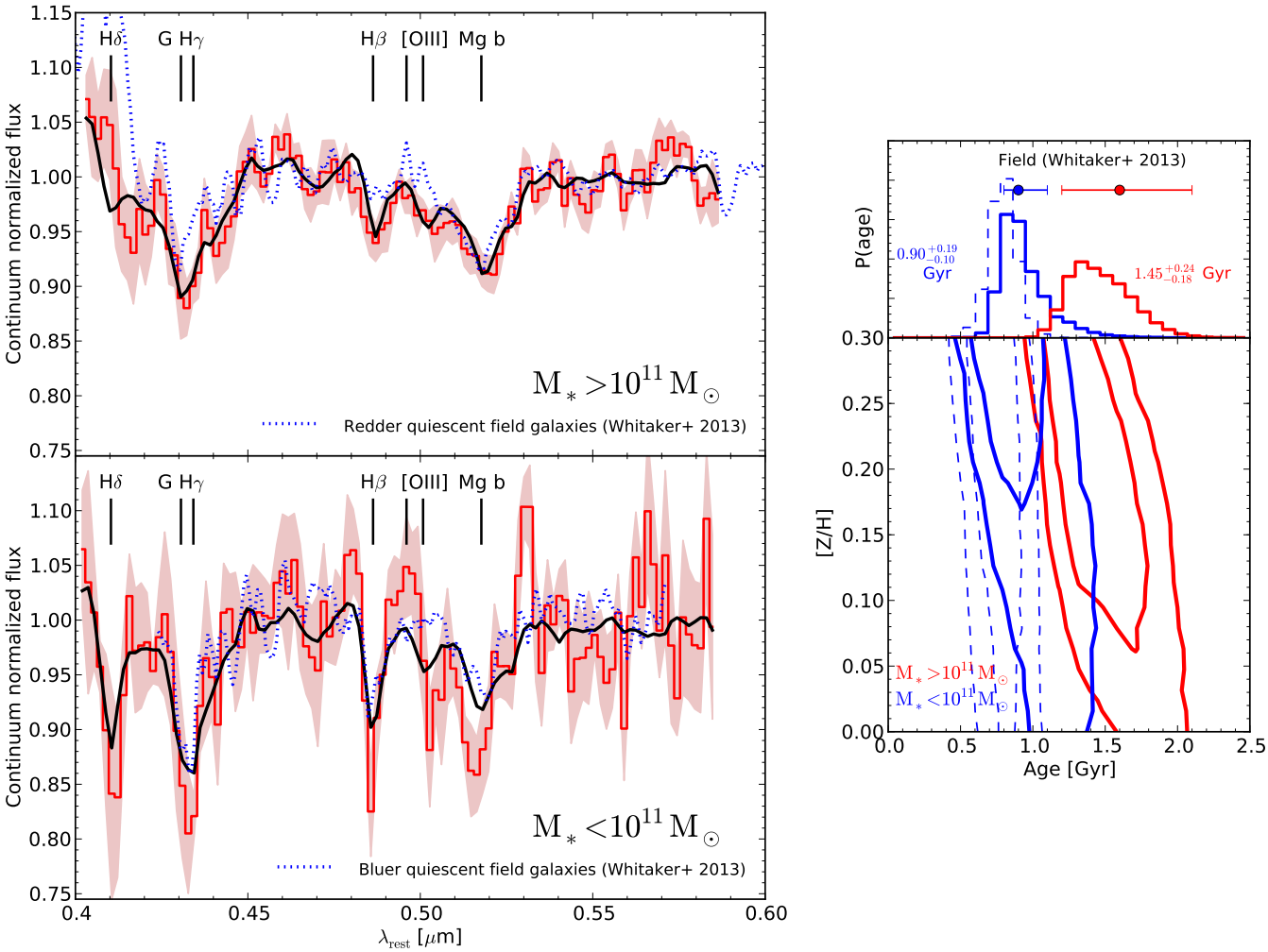

FIG. 9.— **Left:** Composite spectra of confirmed quiescent members of JKCS 041 in two bins of stellar mass. Red curves show the data and 1σ uncertainties, and black lines show the model fit. Dashed blue curves show composite spectra of quiescent field galaxies from Whitaker et al. (2013): the upper and lower panels show their stacks of redder and bluer quiescent galaxies, respectively. **Right:** Constraints on the simple stellar population model derived for the two mass-selected subsamples. Contours show 1σ and 2σ constraints; dashed contours show results for the lower-mass subsample when Mg b is masked. The upper panel shows the marginalized posterior distribution for the age and compares to field constraints derived by Whitaker et al. (2013) for their bluer and redder quiescent galaxy subsamples (1σ error bars).

their bluer subsample as well, although the signal there is more ambiguous. Our stack of lower-mass members shows no clear evidence of emission, but the lower signal-to-noise ratio makes this distinction marginal.

Comparing the ages derived in our two stacks to the Whitaker et al. measurements in the upper right panel of Figure 9, we find that the cluster and field samples span a very similar range. Quantitatively, the differences in luminosity-weighted mean stellar ages are $\Delta t = \mathrm{age}_{\mathrm{JKCS041}} - \mathrm{age}_{\mathrm{field}} = -0.2 \pm 0.5$ Gyr and $0.0^{+0.3}_{-0.1}$ Gyr for the more-massive/redder and less-massive/bluer subsamples, respectively. These results are marginalized over a range of metallicity, whereas Whitaker et al. instead fixed the metallicity to solar abundance in their analysis. If we do the same, these age differences shift to $\Delta t = 0.2 \pm 0.5$ Gyr and $0.3^{+0.3}_{-0.2}$ Gyr, respectively. In this solar metallicity case, however, the age of the lower-mass cluster members is strongly influenced by the Mg b region, where we noted that the fit is poor. Masking Mg b and relying on Balmer line indictors yields $\Delta t = 0.0^{+0.2}_{-0.1}$ Gyr for the lower-mass subsample.

In each of these comparisons, we do not detect a difference between the field and cluster mean ages at the $\sim 1\sigma$ level, or about 0.5 Gyr and 0.3 Gyr for the more- and less-massive subsamples, respectively. Because the median redshift of the galaxies entering the Whitaker et al. stacks is slightly lower than that of JKCS 041, comparing ages is not precisely the same as comparing formation times. However, the difference in median lookback time is ~ 0.3 Gyr for the massive/redder subsample and only 0.1 Gyr for less-massive/bluer examples; both are less than the statistical uncertainties. We also note that the mean ages derived above will not include any galaxies that were very recently truncated and are in transition to the quiescent region of the UVJ plane.

In summary, the mean luminosity-weighted ages of the quiescent members of JKCS 041 varies with mass, with lower-mass galaxies having younger ages. The cluster members span a remarkably similar range of ages to that seen in quiescent field galaxies near the same redshift. Intriguingly, however, the line emission seen in quies-

cent field samples is absent in JKCS 041, at least among its more massive members where the high quality of the spectrum permits a comparison. We discuss the physical significance of these findings in Section 7.

6. STRUCTURE OF QUIESCENT GALAXIES: JKCS 041 COMPARED TO THE FIELD

To gain insight into the role of the environment in the rapid structural evolution of quiescent galaxies at $z \sim 2$, we now compare the structural properties of the members of JKCS 041 to their field counterparts. In addition to our *HST* imaging of the cluster, this comparison requires a large field sample. Furthermore, in order to minimize systematic differences, the structural measurements should be conducted following the same procedures in the cluster and field. The CANDELS data provide an excellent basis for such a comparison, since the survey has imaged a large area using *HST*/WFC3 to a depth similar to our F160W observations. Here we assemble a sample of 225 galaxies spanning $z = 1.8 \pm 0.3$ drawn from the CANDELS fields. Using this large sample, we are able to make a precise and homogeneous comparison between galaxy structure in JKCS 041 and the field.

6.1. *Structural measurements and field sample*

We used `Galfit` to fit two-dimensional Sérsic profiles to the F160W images of all spectroscopically-confirmed quiescent cluster members (Figure 10). The detailed procedures for PSF construction and masking or simultaneous fitting of nearby galaxies follow those described in N12. The only procedural difference is that we estimate the sky in a larger rectangular annulus around the object, with a width of 80 pixels, and mask objects more aggressively when the sky level is estimated. The derived structural parameters are listed in Table 2. Throughout this section, we refer sizes using the semi-major axis $a = R_e^{\rm maj}$ of the ellipse enclosing half of the light, and *not* a "circularized" effective radius $\sqrt{ab}$ that is also frequently quoted in the literature. We prefer $R_e^{\rm maj}$ because it is independent of inclination for oblate objects, which form one focus of our analysis, whereas the circularized radius is very sensitive to viewing angle for flattened systems. For the lowest-mass confirmed quiescent member (ID 255), we were unable to secure a reliable size measurement, since this galaxy is essentially unresolved. Based on our simulations, its size is likely $R_h \lesssim 1$ pixel ≈ 0.5 kpc. Our comparison to the field is limited to galaxies having $M_* > 10^{10.7}\,{\rm M}_\odot$, so this low-mass galaxy does not enter our analysis.

In this section we refer to stellar masses $M_*^{\rm tot}$ that are scaled to the total flux in the Sérsic profile fit. This is preferable when constructing the mass–radius relation, since the size and luminosity are derived consistently from the same light profile. For the largest galaxies, we note that $M_*^{\rm tot}$ can exceed the `MAG_AUTO`-scaled masses $M_*^{\rm AUTO}$ (Table 1) by up to 0.25 dex.

Our field comparison sample is drawn from four of the CANDELS survey fields. We have augmented the UDS and GOODS-S catalogs in N12 by adding data in COSMOS and GOODS-N, where we make use of the NMBS and MOIRCS Deep Survey (Kajisawa et al. 2011) photometry. In each field, photometric redshifts, stellar masses, and rest-frame colors were estimated using the same procedures described in Section 2.2, based throughout on the BC03 models and a Salpeter IMF. Sérsic profiles were fit to the CANDELS F160W images using the same methods applied to JKCS 041. Our field comparison sample consists of 225 galaxies with $M_* > 10^{10.7}\,{\rm M}_\odot$ in the redshift interval $z = 1.8 \pm 0.3$ that are classified as quiescent according to their UVJ colors. Galaxies within 1 Mpc of the known $z = 1.62$ cluster at the edge of the UDS field (Papovich et al. 2010; Tanaka et al. 2010; see Section 7) were removed. For 17 galaxies in the field sample (7.5%) and 1 of the cluster members, the Sérsic index reached the maximum value $n = 8$ allowed in our fits. Since the radii derived in such cases are often unreliable (see N12, Raichoor et al. 2012), we indicate these galaxies separately in our plots and omit the $n = 8$ field galaxies when fitting the mass–radius relation.

TABLE 2
Sérsic fits to confirmed quiescent cluster members

ID	$R_e^{\rm maj}$ (kpc)	q	n	$H_{160}^{\rm tot}$	$\log M_*^{\rm tot}/M_\odot$
272	14.7	0.71	6.8	20.03	11.96
376	5.00	0.70	6.5	20.84	11.70
286	5.27	0.83	8.0	21.17	11.68
356	10.6	0.97	7.7	20.71	11.62
355	4.72	0.56	2.7	20.65	11.58
352	2.45	0.74	5.2	21.56	11.34
411	0.85	0.57	4.1	21.93	11.22
657	1.56	0.91	3.2	21.45	11.18
289	0.83	0.65	3.8	21.97	10.97
447	3.13	0.81	3.3	21.95	10.88
317	1.43	0.47	1.9	22.30	10.81
281	0.89	0.75	3.0	22.61	10.80
375	0.62	0.95	3.4	22.64	10.79
359	1.47	0.86	6.9	22.29	10.77
255	(unresolved — see text)				

Note. — Stellar masses in the final column are scaled to the total Sérsic magnitude and so differ from the `MAG_AUTO`-scaled masses in Table 1. See Section 6.1 for estimates of uncertainties.

To validate our fitting method, we inserted hundreds of simulated galaxies with Sérsic profiles into the UDS and JKCS 041 images with a distribution of parameters similar to that in our sample. We found that n, R_h, and the total flux are recovered with negligible biases, i.e., less than a few percent. The typical 1σ uncertainties in R_h are $\sigma_{R_h} = 10\%$ for the majority of systems having $R_h < 0\farcs5$, increasing to 17% for larger galaxies. In about 7% of cases, R_h differs from the true value by more than factor of 1.5. The Sérsic index n is recovered with errors of $\sigma_n = 0.4$ when $n < 5$, increasing to $\sigma_n = 0.9$ for more extended profiles having $n = 5 - 7$. Total fluxes are recovered with a scatter of $\sigma_{\rm mag} \simeq 0.1$ mag. These estimates can be applied to the measurements in Table 2.

6.2. *Shapes of Quiescent JKCS 041 Members versus the Field*

We begin our structural comparison of quiescent field and cluster galaxies by considering their shapes. Figure 11 compares the projected axis ratios $q = b/a$ of the two samples. The top panel shows that the field sample spans a wide range of shapes that extends to highly flattened systems with low q. This suggests that many quiescent field galaxies at $z \sim 1.8$ harbor a significant disk component. A visual inspection of images of the systems having $q \lesssim 0.5$ supports this conclusion. Other authors have noted evidence of significant disk-like struc-

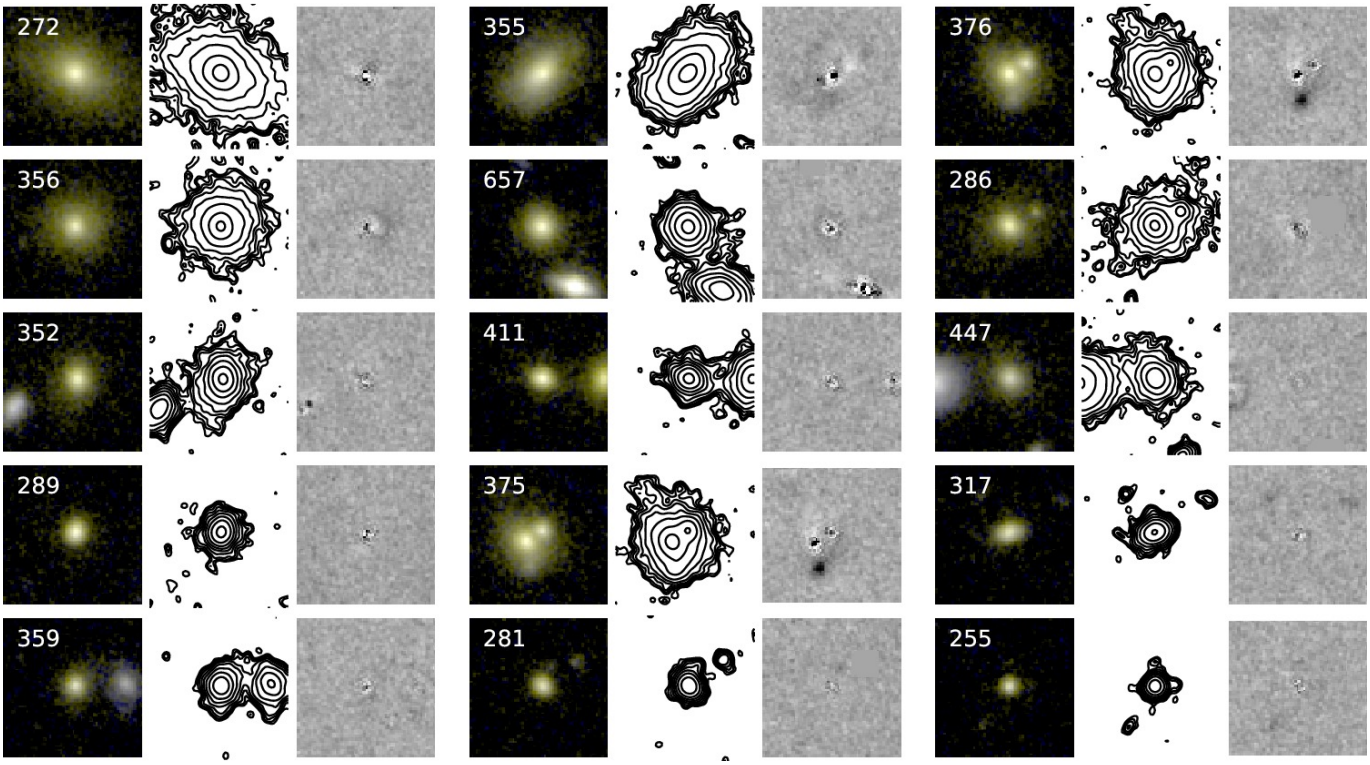

FIG. 10.— F160W/F105W images (left panels) of the 15 confirmed quiescent members of JKCS 041 ordered by F160W flux, displayed with a logarithmic scaling. Center panels show logarithmically-spaced F160W isophotes. Right panels show residuals of the Sérsic fits to each F160W image, scaled linearly over ± 23 mag arcsec^{-2}. Pixels masked in the fits are set to zero. The cutout side length is $4'' \approx 34$ kpc.

tures in quiescent galaxies at $z > 1$, even at the highest stellar masses, based on both their projected axis ratio distribution (van der Wel et al. 2011; Weinzirl et al. 2011; Buitrago et al. 2013; Chang et al. 2013b,a) and on results from two-component bulge/disk decompositions (Stockton et al. 2008; McGrath et al. 2008; Bruce et al. 2012; Papovich et al. 2012)

Turning to the JKCS 041 members in the lower panel of Figure 11, there appear to be fewer flattened galaxies: only one, for example, has $q < 0.5$. Quantitatively, the difference in mean projected axis ratios is $\langle q_{\rm JKCS} \rangle - \langle q_{\rm field} \rangle = 0.11 \pm 0.04$, and we derive a p-value of 0.03 from a permutation test that indicates this difference is moderately significant.[9] This suggests a probable difference in the underlying morphological composition of the cluster and field galaxies.

More physical insight can be gained from the q distribution using a model for the distribution of intrinsic galaxy shapes. Chang et al. (2013b) have shown that the q distribution of quiescent galaxies can be understood as arising from a two-component population viewed at random angles. One component consists of mildly triaxial galaxies that are nearly spherical, and the other consists of a highly flattened, oblate population. In the following, we refer to these as the spheroid and disk-like components, respectively, although it should be kept in mind that the quiescent disk-like galaxies are likely composite objects containing significant bulges (Bruce et al. 2012) and may be related to the lenticular population at lower redshift; we note that these passive disk-like galaxies appear to span a range of Sérsic indices $n \approx 1 - 5$. This decomposition of the q distribution is not unique, but it is motived by more detailed photometric and kinematic classifications at lower redshift and serves as a useful starting point for understanding the $z > 1$ population. Chang et al. showed that the fraction $f_{\rm obl}$ of quiescent systems belonging to the disk-like population appears to be roughly independent of mass over the range of masses and redshifts relevant for the present paper. In support of this, we see no trend in $\langle q \rangle$ with mass in Figure 11.

Overlaid on the histograms in Figure 11 are fits based on this two population model.[10] Figure 12 shows the inferred fraction $f_{\rm obl}$ of disk-like galaxies. We find that about half ($f_{\rm obl} = 0.52 \pm 0.08$) of the $z \sim 1.8$ field sample belongs to the disk-like population, consistent with Chang et al., whereas in JKCS 041 the q distribution is best fit with a pure spheroid population ($f_{\rm obl} = 0$), with $f_{\rm obl} < 0.28$ at 68% confidence. Comparing the two samples, we find that $f_{\rm obl}$ is lower in the cluster at 90% confidence.

6.3. *Sizes and Radial Profiles of Quiescent JKCS 041 Members versus the Field*

The stellar mass–radius relations for the quiescent field galaxies and the quiescent JKCS 041 members are shown in Figure 13. As a first step toward comparing the two, we fit a linear relation with Gaussian scatter $\mathcal{N}(\sigma)$ to the

[9] The p-value is the fraction of random permutations of the field and cluster identifications for which $\langle q_{\rm JKCS} \rangle - \langle q_{\rm field} \rangle$ exceeds that which is observed in absolute value (i.e., a two-sided test).

[10] We use the distribution of intrinsic axis ratios within the oblate and triaxial populations from the first entry in Table 3 of Chang et al. (2013b).

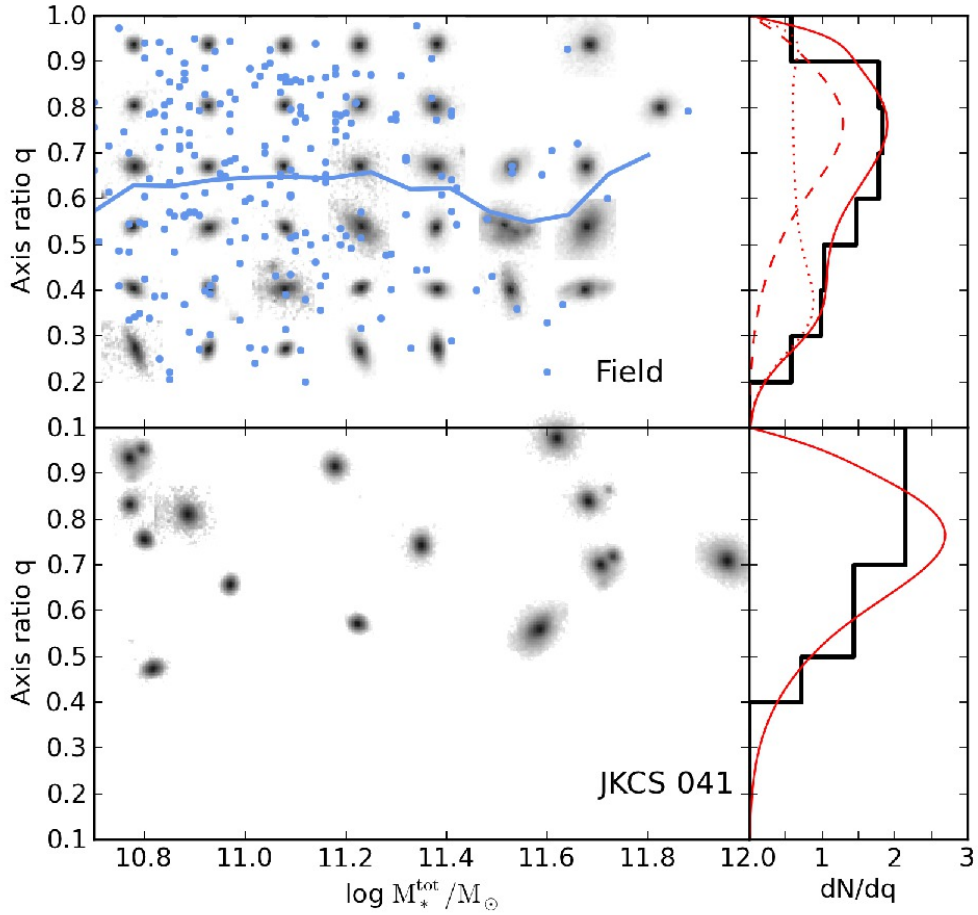

FIG. 11.— Projected axis ratios q as a function of stellar mass for the quiescent galaxies in our field sample (top panel) and in JKCS 041 (bottom). In the top panel, a grid of randomly-selected cutouts having the corresponding M_* and q is shown, with the blue points denoting the actual parameters of the field galaxies and the blue line indicating the running mean. Histograms show the normalized q distributions. Red curves show the best-fitting two-component model described in the text: dotted and dashed curves denote the disk-like, oblate population and the spheroid population, respectively, while solid curves show their sum. The JKCS 041 members are best-fit by a pure spheroid population, whereas about half of the field sample belongs to the oblate population in this model (see Figure 12).

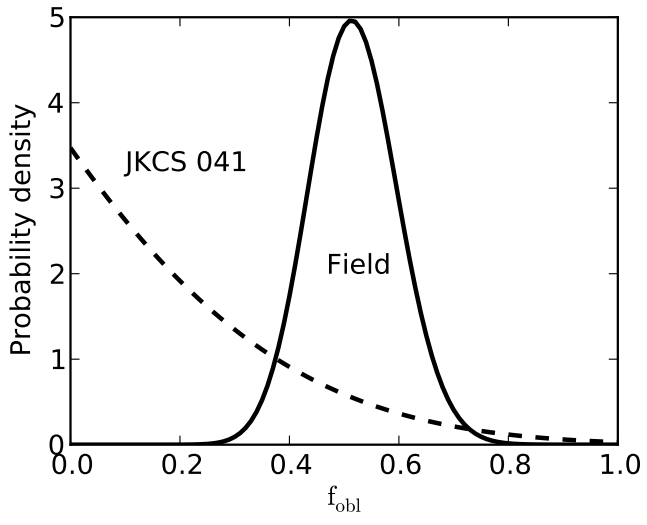

FIG. 12.— Posterior probability density for the fraction f_{obl} of quiescent galaxies that belong to the disk-like, oblate population, based on the model proposed by Chang et al. (2013b).

field sample:

$$\log R_e^{maj}/\mathrm{kpc} = \alpha + \beta \log \mathrm{M}_*^{tot}/10^{11}\mathrm{M}_\odot - 0.26(z-1.8) + \mathcal{N}(\sigma), \quad (1)$$

where $\beta = 0.61 \pm 0.07$, $\alpha = 0.22 \pm 0.02$, and $\sigma = 0.23 \pm 0.01$. Here we have taken into account the mild redshift evolution $\partial \log R/\partial z = -0.26$ expected within field sample based on the results by N12. This fit is shown by the blue line. Comparing the JKCS 041 members to the mean field relation, there is no evidence for a systematic difference between the two: $\langle \Delta \log R_e^{maj} \rangle = 0.01 \pm 0.09$.[11] There is a hint, however, of a mass-dependent trend: the 5 most massive galaxies are all displaced above the mean field relation, by an average $\langle \Delta \log R_e^{maj} \rangle = 0.21 \pm 0.12$.

Since the axis ratio distribution suggests that the morphological mix of quiescent galaxies may be different in JKCS 041 and the field (Section 6.2), it is important to consider what effect this may have on a comparison of

[11] Throughout, the uncertainty in the mean $\langle \Delta \log R_e^{maj} \rangle$ is estimated as $\sqrt{\sigma_{clus}^2 + \sigma_{field}^2}$. Here the uncertainty $\sigma_{clus} = 0.23/\sqrt{N_{clus}}$ in the mean cluster galaxy offset is based on the scatter seen in the field relation (Equation 1), and the uncertainty σ_{field} in the mean field relation is derived from the fit parameters.

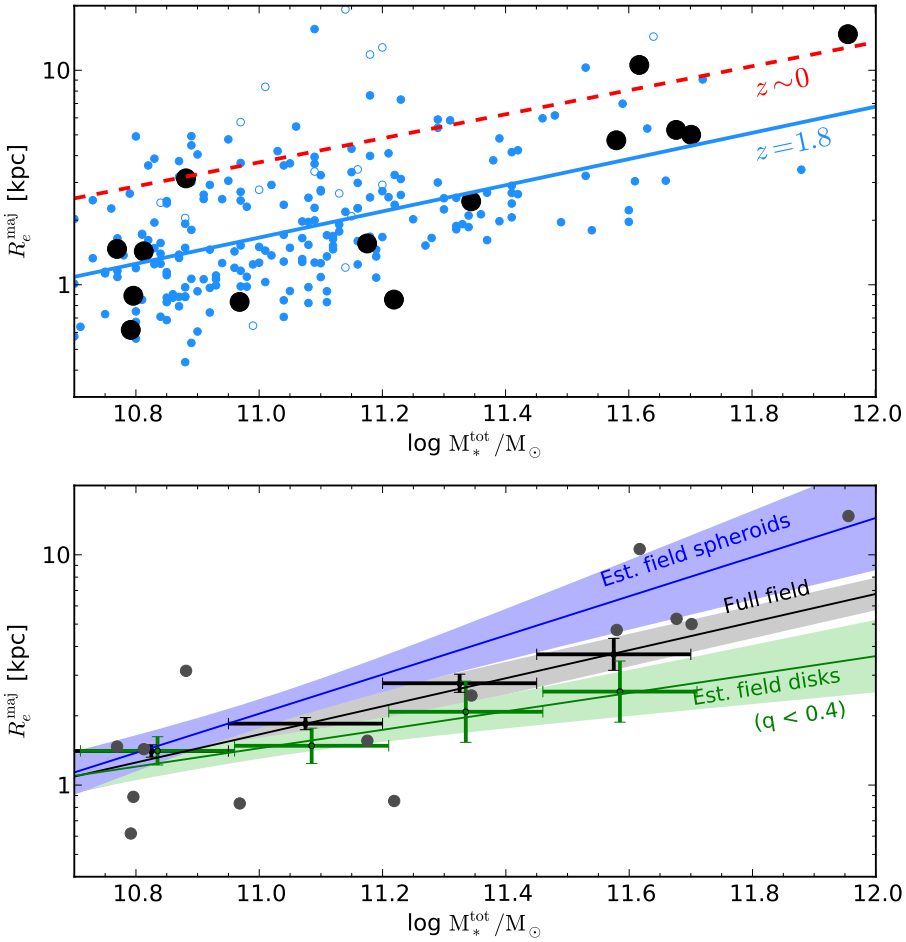

FIG. 13.— **Top:** Stellar mass–$R_e^{\rm maj}$ relation for quiescent galaxies in JKCS 041 (black symbols) and in our $z = 1.8 \pm 0.3$ field sample (blue). The solid line shows the field relation at $z = 1.8$ (Equation 1), and the dashed red line shows the $z \sim 0$ relation for early-type galaxies from Shen et al. (2003), where we have converted their circularized radii to $R_e^{\rm maj}$ estimates by assuming a mean axis ratio of $\langle q \rangle \approx 0.75$ (e.g., Padilla & Strauss 2008). Open symbols denote field galaxies best fit with $n = 8$, whose sizes may be unreliable. **Bottom:** The stellar mass–$R_e^{\rm maj}$ relation for our color-selected sample of quiescent field galaxies (black symbols with error bars) is compared to that defined by the subset of flattened galaxies with $q < 0.4$ (green) and to our inferred relation for the spheroid population (blue). Bands indicate 1σ uncertainties, and grey circles show the JKCS 041 members as in the top panel.

sizes. If the morphological compositions indeed differ, then a simple comparison of radii — such as that performed above — will conflate the sizes of spheroids and disks, rather than isolating the effect of the environment on galaxies of comparable morphologies. While nearly edge-on disk-like galaxies are easily identified, it is not easy to locate the same systems viewed at lower inclination. A division in Sérsic index is not very effective, since flatted ($q \lesssim 0.4$) quiescent galaxies are seen in the field over a wide range of $n \approx 1 - 5$. Therefore, rather than attempting to morphologically classify the individual galaxies in the distant field sample, we proceed from the model of the underlying shape distribution discussed in Section 6.2 and follow its implications for the mass–radius relation.

The lower panel of Figure 13 demonstrates that the flattened quiescent field galaxies having $q < 0.4$ (green symbols) appear to follow a different mass–radius relation: they have smaller $R_e^{\rm maj}$ than the bulk field sample (black symbols), and increasingly so at higher masses.[12] We expect the $q < 0.4$ galaxies to be a fairly pure ($f_{\rm obl} = 0.89$, according to the decomposition in Section 6.2) but incomplete sample of the disk-like population. Since $R_e^{\rm maj}$ is independent of inclination for transparent, oblate objects, those galaxies in the disk-like population that are viewed more nearly face-on, i.e., with higher q, should follow the same mass–radius relation. Assuming that a fraction $f_{\rm obl} = 0.52 \pm 0.08$ of quiescent field galaxies — of all inclinations — belong to this disk-like population, it is then straightforward to estimate the mass–radius relation for the spheroids. Specifically, at each mass we consider the mean $\langle \log R_e^{\rm maj} \rangle$ as a weighted average: $f_{\rm obl}\langle \log R_{e,{\rm obl}}^{\rm maj} \rangle + (1 - f_{\rm obl})\langle \log R_{e,{\rm sph}}^{\rm maj} \rangle$.

The blue band in Figure 13 shows the resulting constraint on the relation for quiescent field spheroids. If

[12] For a single population of triaxial objects, the smallest q is seen when longest and shortest axes are in the plane of the sky, and the projected $R_e^{\rm maj}$ is maximal. The fact that small-q galaxies have *smaller* $R_e^{\rm maj}$ thus supports the notion that they are a distinct population with a different size distribution. We also emphasize that our discussion is confined to *quiescent* galaxies, and star-forming disks are well known to have larger sizes (e.g., Williams et al. 2010, N12, and references therein).

the cluster galaxies are indeed dominated by spheroids, as suggested by their axis ratio distribution, it is clear that any difference between the field and cluster relations at high masses is much reduced. Quantitatively, the sizes of the 5 most massive cluster members do not differ systematically ($\langle \Delta \log R_e^{\rm maj} \rangle = -0.06 \pm 0.19$) from the field spheroid relation, although the uncertainties are necessarily increased, and when considering the full range of masses, the cluster members are slightly smaller but still consistent with the field spheroids ($\langle \Delta \log R_e^{\rm maj} \rangle = -0.14 \pm 0.10$). We regard our morphological separation of the mass–radius relation of quiescent galaxies as a first approximation, since it relies on a very simple model for the underlying distribution of shapes (Section 6.2; Chang et al. 2013b) and its apparent invariance with mass at $z \sim 2$. More data is needed to test this model and its implication that the fraction of massive, quiescent galaxies with significant disk components increases with redshift. However, it is clear that a difference in the morphological mixtures of the field and cluster samples could significantly affect comparisons of their mass–radius relations.

In summary, there is no significant difference overall between the mass–radius relation defined by the quiescent JKCS 041 members and that defined by our coeval field sample. There is a weak hint of a mass-dependent trend in which the most massive cluster members are offset to larger radii, if all color-selected quiescent galaxies are considered irrespective of morphology. However, a closer inspection reveals that this may arise because the cluster population is richer in spheroids, and spheroids are "larger" than quiescent disk-like galaxies. Figure 14 supports this conclusion via a direct comparison the surface mass density profiles of the JKCS 041 members to the field galaxies. Here we consider only field galaxies with $q > 0.45$ to better match the cluster sample. The *HST* PSF was deconvolved from the observed F160W light profile using the technique proposed by Szomoru et al. (2010), and the resulting light profile was converted to a stellar mass profile using a constant M_*/L for each galaxy. There is no clear difference in the mass profiles in the field and JKCS 041 samples.

6.4. *Comparison to other studies of the environmental dependence of the mass–radius relation*

Several recent studies of the environmental dependence of galaxy sizes at high redshifts are compared in Figure 15. The references in the upper-left legend refer to individual clusters, for which we have compiled published structural measurements of their quiescent or early-type members. In Section 7 we review the bulk physical properties of the $z > 1.6$ clusters themselves; our focus here on the mass–radius relation. To synthesize these published results into a quantity that can be compared as directly as possible, given the diversity of samples and methods (see Appendix C for details), we compute the mean offset $\langle \Delta \log R_e^{\rm maj} \rangle$ between the quiescent members of each cluster and the field relation in Equation 1. We regard Figure 15 as a first step toward synthesizing results from various high-z studies, but caution that systematic differences in measurement techniques may affect a comparison of our field sample with other authors' cluster data; some of these are discussed in Appendix C.

Considering the $z > 1.6$ clusters first, Papovich et al. (2012, see also Bassett et al. 2013), Zirm et al. (2012) and Strazzullo et al. (2013) have all remarked on evidence for larger sizes among the quiescent members of the clusters they studied. (We note that many of these members are actually photometric candidates, whereas the members of JKCS 041 are confirmed by grism redshifts.) Based on Figure 15, we regard the present evidence for a variation in the mass–size relation in the cores of these most distant clusters and proto-clusters as very marginal. On the other hand, present sample sizes are too small to rule

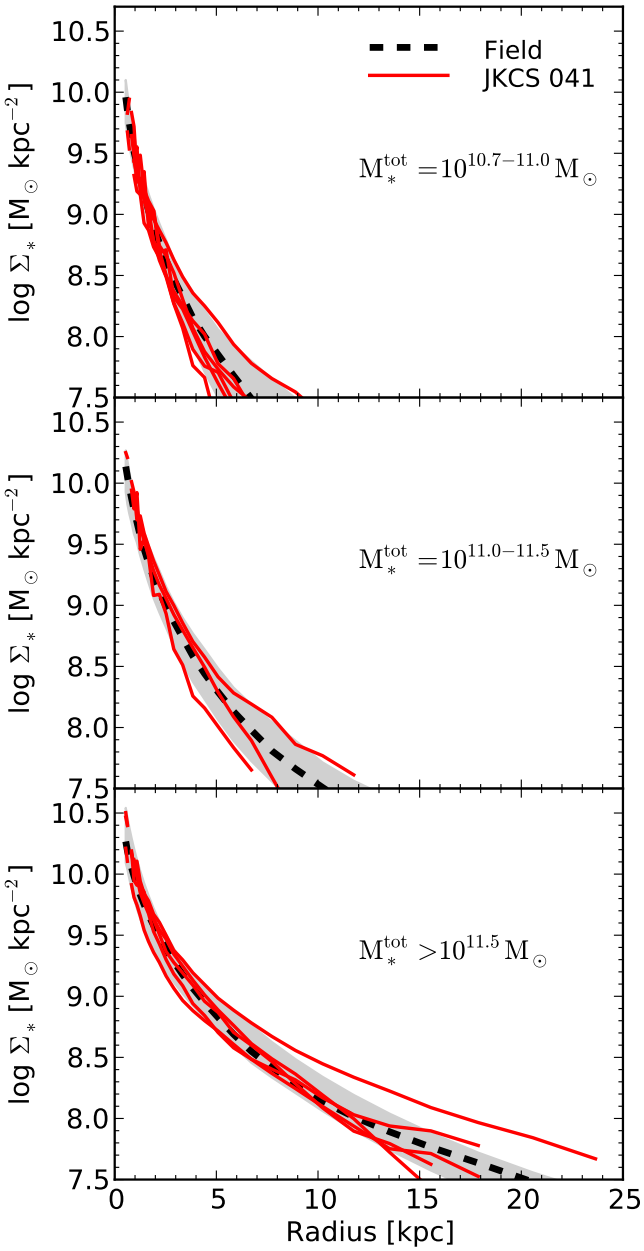

FIG. 14.— Azimuthally-averaged surface mass density Σ_* profiles of JKCS 041 members (red lines), plotted down to a limiting surface brightness of $H_{160} = 26$ mag arcsec^{-2} and PSF-deconvolved as described in the text. In each of 3 stellar mass bins, we compare to the population of quiescent field galaxies at $z \sim 1.8$ that have $q > 0.45$, excluding highly flattened galaxies that are absent in the cluster sample. The thick dashed line shows median surface density profile of the field sample derived from our Sérsic fits, and the grey region encloses 68% of the field profiles at each radius.

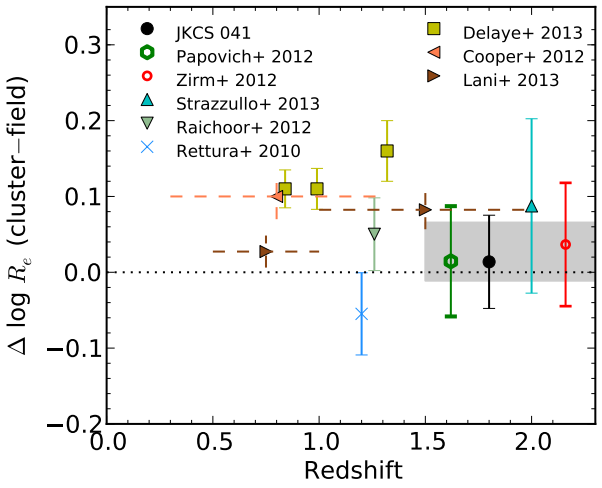

FIG. 15.— Comparison of published results on the environmental dependence of the mass–radius relation of quiescent galaxies. Each point represents the mean offset $\Delta \log R_e$ from the field relation. For studies of individual clusters, listed in the upper-left legend, we compare to Equation 1. For ensembles of clusters (Delaye et al. 2013) and studies of group-scale overdensities (Cooper et al. 2012; Lani et al. 2013, dashed error bars), the published offsets from the authors' field relation are quoted directly. The shaded band denotes the weighted mean of the $z > 1.6$ clusters and its 1σ uncertainty. Appendix C describes our method for compiling and harmonizing these diverse data sets and describes systematic uncertainties inherent in such a comparison.

out a modest size enhancement of ~ 0.05 dex. Moving to lower redshifts, Delaye et al. (2013) studied 9 clusters at $z = 0.8 - 1.4$ along with a field sample selected and analyzed in a homogeneous way. They found significant evidence for an offset in the mass–radius relation by $\Delta \log R_e \simeq 0.1$ dex. In the two $z \sim 1.2$ clusters studied by Rettura et al. (2010) and Raichoor et al. (2012), however, we find no significant offset.

Bassett et al. (2013) noticed that the slight trend for the quiescent candidate members of the cluster they studied (IRC-0218A, $z = 1.62$) to have larger R_e and smaller n was mostly driven by a population of disk galaxies located at large cluster-centric radii $R \approx 1 - 1.5$ Mpc.[13] Although their remark that differences in morphology can influence comparisons of the mass–radius relation is similar to our findings, we note that that the nearly pure disks they discuss ($n \sim 1$) have *larger* R_e than the mean quiescent galaxy — consistent with faded spirals that have been starved of gas during infall — whereas the disk-like quiescent field population discussed in Section 6.3 is offset to *smaller* R_e and exhibits a wide range of n indicating a significant build-up of bulges (see a similar trend in Huertas-Company et al. 2013). Altogether, this points to a complex mixture of morphologies varying from the field to the cluster outskirts and core.

In addition to these cluster studies, two recent studies have examined the dependence of the mass–radius relation on local density in blank field surveys, where the densest regions are typically groups. These results are distinguished with dashed error bars in Figure 15. Cooper et al. (2012) found a size enhancement of $\Delta \log R_e \simeq 0.1$ dex among early-type galaxies in the densest regions in the DEEP3 survey fields. In the UDS field, Lani et al. (2013) detected a similar enhancement that was dominated by the most massive and highest-redshift galaxies. This is the regime where we found that differences in the morphological mix could affect our interpretation of JKCS 041. Lani et al. considered such a possibility and tested it by cutting their sample in Sérsic index n. Although this is a reasonable first approach, we find the connection between the oblate, disk-like quiescent population and Sérsic index to be loose (Section 6.3). Additionally, while the M_*–$R_e^{\rm maj}$ relation likely varies with q (Figure 13), we find no such dependence on n for quiescent galaxies. In future work, it would be useful to consider the q distributions of samples whose mass–radius relations are being compared.

In contrast to these $z \gtrsim 1$ studies, there appears to be *no* dependence at $z \sim 0$ of the size of early-type galaxies on local density, halo mass, or position within the halo (Weinmann et al. 2009; Guo et al. 2009; Nair et al. 2010; Huertas-Company et al. 2012). These $z \sim 0$ results, however, have been challenged by Valentinuzzi et al. (2010), who claim an excess of *compact* massive galaxies in local clusters; interestingly, these compact galaxies show a tendency to have S0 morphologies. The only clear point of agreement is that the BCGs in very massive clusters are exceptionally large (e.g., Bernardi et al. 2007).

In summary, the evidence for environmental variation in the mass–radius relation in the most distant $z > 1.6$ clusters is still limited by small samples. At $z \sim 1$ there is good evidence for an offset to larger sizes in the cluster sample studied by Delaye et al. (2013), as well as in group-scale overdensities (Cooper et al. 2012; Lani et al. 2013). At $z \sim 0$, most evidence points toward a remarkable independence of early-type galaxy structure on environment. There are contrary indications for many secondary trends that might shed light on an underlying physical picture: are galaxy sizes enhanced primarily in distant clusters' cores (Delaye et al.) or their outskirts (Bassett et al. 2013)? Is the enhancement stronger for higher (Lani et al.) or lower mass (Delaye et al.) galaxies? Furthermore, the evolutionary connection between $z \gtrsim 1$ results and the precise constraints available at $z \sim 0$ remains unclear.

7. DISCUSSION

In addition to JKCS 041, 7 overdensities containing a red galaxy population have been identified at $z > 1.6$ and confirmed spectroscopically.[14] Although all have been labeled "clusters" or "proto-clusters," these are in fact a diverse set of structures that span a wide range of masses and evolutionary states. The properties of these systems are summarized in Table 3. JKCS 041 is remarkable in several ways. It is among the most X-ray luminous clusters known at such a high redshift. Correspondingly, although the uncertainties in mass are large, JKCS 041 appears to be as massive as any known cluster at $z > 1.6$, with IDCS J1426+3508 (Stanford et al. 2012) being the closest analogue in mass and X-ray lumi-

[13] As described in Appendix C, we include only the members of this cluster within $R < 1$ Mpc in Figure 15 for a better comparison with other data sets.

[14] In addition to these, we note that Spitler et al. (2012) recently discovered a $z = 2.2$ cluster candidate containing a red galaxy population.

TABLE 3
JKCS 041 Compared to Other Spectroscopically Verified $z > 1.6$ Proto-Clusters and Clusters

Cluster	z	Mass ($M_\odot$)	Diffuse X-ray flux (erg cm^{-2} s^{-1})	$N_{\rm spec}$ / $N_{\rm spec\ Q}$	References
JKCS 041†	1.80	$M_{500} = 2.9^{+3.8}_{-2.4} \times 10^{14}$	2×10^{-14}	19 / 15	This work, refs. in §1
IRC-0218A *	1.62	$M_{200} \simeq (2-7) \times 10^{13}$	$\sim 3 \times 10^{-15}$	11 / 3	P10, T10, P12, B13, L13, Pi12
SpARCS J022427-032354	1.63	...	...	12 / 3	Muzzin et al. (2013)
IDCS J1426+3508†	1.75	$M_{500} \simeq 3 \times 10^{14}$	3×10^{-14}	7 / 2	Stanford et al. (2012)
IDCS J1433.2+3306†	1.89	$\simeq 10^{14}$	...	7 / 2	Zeimann et al. (2012)
Cl J1449+0856†	2.00	5×10^{13}	9×10^{-16}	22 / 7	G11, G13, S13
MRC 0156-252	2.02	...	$\sim 2 \times 10^{-15}$‡	10 / 1	O05, Ga13
MRC 1138-262	2.16	...	...	11 / 4	Z12, T13, and references therein

Note. — $N_{\rm spec}$ is the number of spectroscopic members, of which $N_{\rm spec\ Q}$ are quiescent. Masses and X-ray fluxes are only indicative, since various energy bands, apertures, and scaling relations are used. References: P10, P12: Papovich et al. (2010, 2012), Pi12: Pierre et al. (2012), G11, G13: Gobat et al. (2011, 2013), S13: Strazzullo et al. (2013), T10, T13: Tanaka et al. (2010, 2013), B13: Bassett et al. (2013), L13: Lotz et al. (2013), Z12: Zirm et al. (2012), O05: Overzier et al. (2005), Ga13: Galametz et al. (2013). †Based on WFC3 grism data. *Also called XMM-LSS J02182-05102. ‡The X-ray emission is suspected to be associated with the radio galaxy rather than thermal ICM emission.

nosity. The large number of very massive, red galaxies we have confirmed as members of JKCS 041 supports this conclusion: its most massive 3 members, for example, all outweigh the most massive candidate member of Cl J1449 or MRC 1138-262 (see references in Table 3).

Motivated by the abundance of quiescent galaxies in JKCS 041, we have compared their structural and stellar population properties to coeval field samples. Considering first the structure and morphology of the cluster members, we found some evidence for a lack of quiescent disk-like galaxies relative to the field population. In the context of cluster studies at lower redshift, this is consistent with the idea that the cluster ellipticals are formed early ($z > 2$) in dissipative mergers, probably continuing to evolve via dry mergers, whereas many S0's are formed much later at $z \lesssim 0.5$ and decline in numbers toward higher redshifts (e.g., Dressler et al. 1997; Andreon et al. 1997; Postman et al. 2005; Poggianti et al. 2009). An interesting related development is the observation that the fraction of quiescent galaxies in the field with disk-like components appears to *increase* at $z > 1$, particular among massive ($M_* > 10^{11}\,M_\odot$) systems (see references in Section 6.2). The relative lack of these compact, disk-like quiescent galaxies in JKCS 041 suggests that the cluster environment either inhibits their formation or else is effective in destroying the more loosely-bound disk material, perhaps through tidal stripping or galaxy–galaxy encounters that build up the bulge. Larger samples are needed to verify this trend, particularly in distant clusters with a well-developed ICM as in JKCS 041.

Comparing the radial profiles of the cluster members to their field counterparts, we detect no statistically significant differences overall, but found a hint of a trend for larger effective radii among the most massive cluster members. One interpretation, which has been promoted in studies of other $z > 1.6$ clusters and proto-clusters (Zirm et al. 2012; Papovich et al. 2012; Bassett et al. 2013; Lotz et al. 2013), is that size growth proceeds at an accelerated rate in the cluster environment, perhaps due to a higher rate of mergers or a higher fraction that are dry. We cannot rule out this possibility, but we note that present constraints in these most distant clusters remain statistically weak (Section 6.4). Furthermore, in the case of JKCS 041, we found that a difference in the morphological mixture of color-selected quiescent galaxies relative to the field may account for our observations just as well. Although this explanation also points toward environment-dependent evolution, it suggests a more nuanced picture in which bulge growth and morphological transformation may play a role in shaping the mass–radius relation in clusters, and not only a pure acceleration of "inside-out" spheroid growth.

A weak environmental dependence of size among quiescent galaxies of the same mass and morphology would indicate that either the galaxy merger rate does not vary substantially among the environments sampled, or that the rate of size growth is decoupled from the merger activity. This would be surprising given that mergers are thought to be the prime driver of spheroid growth (see §1). Presently, however, it is not clear how to connect observations of the mass–radius relation in clusters at different redshifts into an evolutionary sequence. As discussed in Section 6.4, results at $z \gtrsim 1.5$ are not conclusive, the $z \sim 1$ study with the most statistical power (Delaye et al. 2013) indicates that cluster members are enlarged by $\Delta \log R_e \approx 0.1$ dex, while at $z \sim 0$ there seems to be no relation between the structure of early-type galaxies and their local environment or halo mass. One possibility is that cluster members experience an initially enhanced rate of galaxy-galaxy encounters and mergers during infall, as the cluster is forming, while the virialization of the cluster and the resulting high velocity dispersion then inhibits future merging (see, e.g., Lotz et al. 2013 and Delaye et al. 2013). In this picture, the mass–radius relation of cluster members is offset to larger R_e at high redshift, while at later times the field galaxies "catch up" and this offset declines. It will be interesting to test this hypothesis as larger samples of distant clusters and richer data sets become available.

While high-z studies have used local density or cluster membership to quantify the environment, a galaxy's status as central galaxy in its dark matter halo may be more physically relevant. Central galaxies are expected grow more rapidly than satellites in some models, and they benefit from the accretion of stars that are tidally stripped from disrupted sinking satellites (e.g., Shankar et al. 2013). This process of "cannibalism" becomes increasingly important in higher halo mass, with the giant

BCGs being the most extreme examples. The BCG of JKCS 041 indeed has the most extended light profile of all the cluster members, and it is the third nearest of the spectroscopic members to the cluster center. The BCG appears similar to that of the massive Stanford et al. (2012) cluster at $z = 1.75$, which is also exceptionally luminous and extended ($R_e = 18$ kpc).

A complementary approach is to quantify the rate of galaxy interactions and mergers more directly. Lotz et al. (2013) indeed inferred a high ongoing merger rate — exceeding that in the field by a factor of 3–10 — in XMM-LSS J02182-05102 at $z = 1.62$, based on their estimation that 57^{+13}_{-14}% of the massive proto-cluster members have double nuclei or a close satellite galaxy. By visual inspection of the 17 spectroscopic members of JKCS 041 in our continuum-selected sample (Figure 10), we find that 3, i.e., 18^{+12}_{-6}%, have close companions within the same search radius used by Lotz et al. (20 kpc comoving).[15] Although a full analysis would require accounting for projected pairs in the cluster, this suggests a lower rate of ongoing mergers in JKCS 041, consistent with the latter being in a more dynamically evolved state.

Turning to the stellar populations of the galaxies in JKCS 041, we found a high fraction of quenched systems compared to coeval field galaxies of the same mass (Figure 8). Elevated quiescent fractions, indicating the early onset of a star-formation–density relation, have been reported in other $z > 1.6$ clusters (e.g., Quadri et al. 2012; Strazzullo et al. 2013). The fraction of quenched galaxies is variable, which is expected when considering forming clusters having a wide range of masses and diverse evolutionary states. JKCS 041 appears to be particularly quiescent compared to the other clusters and proto-clusters listed in Table 3. This may be linked to the clear presence of a hot ICM in JKCS 041.

When considering the physical processes responsible for truncating star formation, it is common to distinguish internal quenching mechanisms (often referred to as mass- or self-quenching) from environmentally-related processes that correlate with the local density or the position of a galaxy within its halo (e.g., Peng et al. 2010). The clear signature of the environment on star-formation activity in JKCS 041 at $z = 1.8$ implies that truncation by cluster processes has been fairly rapid, since the galaxies must have fallen into the cluster fairly recently (see also Quadri et al. 2012). Some semi-analytic models in fact predict the disappearance of environmental quenching beyond $z \gtrsim 1.5$ (McGee et al. 2009), when the ~ 2 Gyr timescale for stripping of hot halo gas ("strangulation") exceeds the time for which the necessary dense ICM has existed. Observations of a star formation–density relation at earlier epochs suggests that more rapid quenching mechanisms may be at work.

Although roughly half of the spectroscopic members of JKCS 041 have been quenched by cluster-related processes (Section 5.1), we nonetheless found that the mean ages of these galaxies does not differ greatly from similarly-selected samples in the field. This indicates that the quenching mechanism had no large effect on *when* truncation occurred. This finding is consistent with the idea that the environment modulates the *fraction* of quiescent systems without much affecting their ages. Evidence at lower redshift for a null or weak ($\lesssim 0.4$ Gyr) environmental dependence of age among quiescent systems comes from studies of spectroscopic age diagnostics (Thomas et al. 2010; Moresco et al. 2010; Muzzin et al. 2012) and spectral energy distributions (Andreon 1996; Raichoor et al. 2011) at $z \simeq 0 - 1.2$, as well as from the evolution of the fundamental plane in clusters and the field at $z < 1.3$ (van Dokkum & van der Marel 2007). Our study extends earlier work by probing cluster galaxy ages through spectral diagnostics close to the epoch of their star formation and comparing these to similar observations of coeval field systems.

There are no AGN members with bright optical line emission in the core of JKCS 041, as are present in several other $z > 1.6$ clusters (e.g., Stanford et al. 2012; Zeimann et al. 2012; Gobat et al. 2013). Much fainter line emission can be reached in our composite spectra. Interestingly, there is no sign of the centrally-concentrated, faint emission in Hβ and [O III] that was seen by Whitaker et al. (2013) in their composite spectra of quiescent field galaxies. Equally strong line emission would have been detected in our stack of $M_* > 10^{11}\,\mathrm{M}_\odot$ cluster members. If the field emission traces star formation, this finding would indicate that the dead cluster members lack the residual nuclear star formation present in field samples. Whitaker et al. suggest that a LINER-type spectrum is more likely, given their estimate of the [O III]/Hβ line ratio and the line luminosity. At $z \sim 0$ the prevalence of faint [O III] emission does not decrease in denser environments (Kauffmann et al. 2004), so such a trend at $z \sim 2$ would be intriguing if verified in other clusters.

8. SUMMARY

Based on our *HST* WFC3 imaging and grism observations of JKCS 041, along with associated multi-wavelength data, we conclude:

1. JKCS 041 is a genuine rich, X-ray luminous cluster at $z = 1.80$, confirmed through the spectroscopic identification of 19 members that are spatially aligned with diffuse X-ray emission. The spectroscopic members include 15 quiescent galaxies, the largest number yet confirmed in any $z > 1.6$ cluster. Five of these are very massive galaxies having $M_*^{\mathrm{tot}} = 10^{11.6-12}\,\mathrm{M}_\odot$.

2. High-quality composite grism spectra of the quiescent cluster members allow us to measure their stellar ages via the strengths of the Hδ, Hγ, Hβ and Mg b absorption lines. Less massive quiescent members with $M_* < 10^{11}\,\mathrm{M}_\odot$ have mean luminosity-weighted ages of $0.9^{+0.2}_{-0.1}$ Gyr, while more massive galaxies are older ($1.4^{+0.3}_{-0.2}$ Gyr).

3. Comparing the spectra of the quiescent cluster members to those of similarly-selected field galaxies studied by Whitaker et al. (2013), we find that the field and cluster samples span a very similar range of ages. At the same time, the fraction of quenched galaxies at fixed stellar mass is much higher in JKCS 041. This implies that the cluster environment is responsible for quenching of a substantial

[15] These are IDs 376 and 375, which are paired with one another and a faint, diffuse blue system (see Figure 10), and ID 286.

fraction of massive galaxies in JKCS 041, but that the mode of quenching (environmental versus internal) does not have a large effect on *when* star formation is truncated within the $\sim 0.3 - 0.5$ Gyr uncertainties in our comparison.

4. The centrally-concentrated Hβ and [O III] emission seen by Whitaker et al. in median spectra of quiescent field galaxies is absent in the JKCS 041 members, at least among the more massive galaxies ($M_* > 10^{11}\,M_\odot$) where the high quality of the grism spectra permit a detailed comparison.

5. Comparing the quiescent members of JKCS 041 to a large sample of coeval field galaxies, we find that the distribution of projected axis ratios suggests a lower fraction of disk-like systems among quiescent galaxies in the cluster.

6. We find no statistically significant difference in the mass–radius relation or in the radial mass profiles of the quiescent cluster members compared to their field counterparts. While the most massive cluster members ($M_* > 10^{11.5} M_\odot$) are marginally offset from the field mass–radius relation when considering all quiescent systems together, this apparent difference is weakened when the samples are better matched in morphology. Larger samples are still needed to clarify the structure of galaxies in distant, forming clusters, as well as to connect these results to studies at lower redshift.

The authors acknowledge insightful conversations with Marc Huertas-Company and Sirio Belli. We also thank Kate Whitaker, Alessandro Rettura, Andrew Zirm, and Casey Papovich for sharing their data in an electronic format, as well as Nor Pirzkal and Beth Perriello for their assistance in planning and executing the *HST* observations. Based on observations made with the NASA/ESA Hubble Space Telescope, obtained at the Space Telescope Science Institute, which is operated by the Association of Universities for Research in Astronomy, Inc., under NASA contract NAS 5-26555. These observations are associated with program number GO-12927, which was supported under NASA contract NAS 5-26555. A.R. acknowledges financial contribution from the agreement ASI-INAF I/009/10/0 and from Osservatorio Astronomico di Brera. Based on observations obtained with MegaPrime/MegaCam, a joint project of CFHT and CEA/IRFU, at the Canada-France-Hawaii Telescope (CFHT) which is operated by the National Research Council (NRC) of Canada, the Institut National des Science de l'Univers of the Centre National de la Recherche Scientifique (CNRS) of France, and the University of Hawaii. This work is based in part on data products produced at Terapix available at the Canadian Astronomy Data Centre as part of the Canada-France-Hawaii Telescope Legacy Survey, a collaborative project of NRC and CNRS.

APPENDIX

A. GRISM REDSHIFT CATALOG

Table 4 lists the redshifts derived for the 98 galaxies described in Section 3. For emission line sources, we assign a quality flag 'A' when more than one line is visible and 'B' otherwise. For continuum sources, we qualitatively assign a quality flag based on the appearance of the spectrum and the posterior probability distribution $P(z)$. Spectra with a weak or absent continuum break, often with a multimodal $P(z)$, carry a 'C' flag. The 'B' flag corresponds to a more clearly detected continuum break; we expect the vast majority of these redshifts to be reliable. The 'A' flag is reserved for the highest signal-to-noise objects with unambiguous continuum breaks and, in some cases, absorption lines.

TABLE 4
Grism Redshifts

ID	R.A.	Dec.	H_{160}	$z_{\rm grism}$	Type	Quality
220	36.695309	−4.687007	19.08	0.285 ± 0.005	E	B
167	36.694981	−4.685004	20.15	1.064 ± 0.005	E	B
698	36.673634	−4.704338	20.18	1.127 ± 0.005	E	B
13	36.683534	−4.672097	20.39	0.609 ± 0.005	E	B
516	36.683296	−4.698129	20.59	0.963 ± 0.005	E	B
272	36.681727	−4.689340	20.63	1.798 ± 0.002	C	A
355	36.686442	−4.692394	20.80	1.798 ± 0.002	C	A
409	36.692244	−4.693913	20.85	0.692 ± 0.005	E	A
60	36.687740	−4.677383	20.86	0.608 ± 0.005	E	B
448	36.691822	−4.694914	21.05	0.797 ± 0.005	E	B
376	36.675006	−4.692865	21.20	1.811 ± 0.006	C	A
64	36.675602	−4.677701	21.24	2.415 ± 0.001	C	A
628	36.678489	−4.701768	21.26	1.592 ± 0.010	C	B
499	36.681694	−4.697093	21.27	1.127 ± 0.005	E	B
445	36.673416	−4.694926	21.33	0.893 ± 0.005	E	B
356	36.694233	−4.692351	21.35	1.805 ± 0.004	C	A
546	36.665075	−4.699060	21.36	2.187 ± 0.054	C	C
485	36.670279	−4.696597	21.41	1.131 ± 0.005	E	B
164	36.661774	−4.684718	21.45	1.325 ± 0.005	E	B
743	36.697722	−4.705844	21.47	1.324 ± 0.003	C	B
657	36.675567	−4.702566	21.61	1.812 ± 0.002	C	A
48	36.678011	−4.676309	21.67	0.962 ± 0.005	E	B
165	36.661849	−4.684869	21.68	1.302 ± 0.005	E	B
286	36.687899	−4.689939	21.69	1.798 ± 0.041	C	B

TABLE 4 — *Continued*

ID	R.A.	Dec.	H_{160}	$z_{\rm grism}$	Type	Quality
342	36.696650	−4.691744	21.74	1.323 ± 0.005	E	A
519	36.702752	−4.697865	21.76	1.055 ± 0.005	E	B
352	36.690511	−4.692148	21.88	1.797 ± 0.005	C	A
601	36.689218	−4.700765	21.89	1.339 ± 0.018	C	C
451	36.680181	−4.695045	21.90	1.470 ± 0.047	C	C
556	36.675557	−4.699295	21.91	1.591 ± 0.006	C	A
249	36.702231	−4.688053	21.98	1.935 ± 0.003	C	A
410	36.673327	−4.693843	22.00	2.406 ± 0.009	C	A
107	36.676193	−4.681298	22.01	1.623 ± 0.004	C	B
452	36.683320	−4.695092	22.02	1.464 ± 0.004	C	A
779	36.695368	−4.707747	22.03	1.713 ± 0.009	C	B
320	36.668857	−4.691090	22.04	1.125 ± 0.005	E	A
411	36.673819	−4.693840	22.11	1.821 ± 0.004	C	A
447	36.691213	−4.694868	22.12	1.797 ± 0.010	C	A
197	36.699141	−4.685847	22.13	1.704 ± 0.007	C	B
166	36.695278	−4.685600	22.16	0.484 ± 0.005	E	B
289	36.689652	−4.689939	22.17	1.802 ± 0.003	C	A
589	36.693715	−4.698247	22.21	0.702 ± 0.005	E	B
392	36.685294	−4.693101	22.33	2.065 ± 0.012	C	B
85	36.689254	−4.679838	22.35	1.519 ± 0.005	E	A
387	36.682313	−4.692964	22.36	1.801 ± 0.009	C	B
655	36.682254	−4.702452	22.40	0.795 ± 0.005	E	B
375	36.674884	−4.692784	22.43	1.819 ± 0.008	C	B
317	36.699109	−4.690911	22.45	1.787 ± 0.003	C	A
80	36.690513	−4.679514	22.51	1.174 ± 0.005	E	A
798	36.667559	−4.708978	22.51	1.065 ± 0.005	E	B
105	36.676666	−4.681000	22.54	1.623 ± 0.004	C	B
359	36.676956	−4.692278	22.54	1.792 ± 0.004	C	B
365	36.691019	−4.692373	22.54	1.511 ± 0.005	E	A
569	36.681467	−4.699630	22.61	1.834 ± 0.022	C	C
637	36.679943	−4.701682	22.70	1.490 ± 0.094	C	C
385	36.702109	−4.692868	22.71	1.257 ± 0.005	E	B
281	36.690609	−4.689444	22.77	1.806 ± 0.004	C	B
334	36.690954	−4.691279	22.79	1.133 ± 0.005	E	B
674	36.687376	−4.703028	22.85	1.302 ± 0.005	E	A
693	36.677710	−4.703786	22.86	1.820 ± 0.014	C	C
323	36.674250	−4.691128	22.99	1.369 ± 0.009	C	C
224	36.684922	−4.686954	23.04	0.966 ± 0.005	E	A
201	36.676671	−4.686139	23.04	0.924 ± 0.005	E	A
8	36.680094	−4.670625	23.07	0.968 ± 0.005	E	A
16	36.692232	−4.672568	23.12	1.474 ± 0.005	E	A
531	36.679186	−4.698393	23.12	1.818 ± 0.005	E	A
414	36.696719	−4.693920	23.16	1.334 ± 0.005	E	A
459	36.675068	−4.695578	23.25	1.599 ± 0.053	C	C
653	36.676695	−4.702391	23.25	1.611 ± 0.041	C	C
368	36.679813	−4.692496	23.26	1.951 ± 0.033	C	C
587	36.665178	−4.700129	23.27	1.917 ± 0.015	C	C
446	36.679765	−4.694762	23.29	1.485 ± 0.054	C	C
255	36.687932	−4.688383	23.30	1.795 ± 0.040	C	C
77	36.681823	−4.678888	23.35	0.902 ± 0.005	E	A
300	36.696786	−4.690403	23.36	0.693 ± 0.005	E	A
582	36.691929	−4.700078	23.42	1.132 ± 0.005	E	A
161	36.684522	−4.684455	23.48	1.137 ± 0.005	E	B
61	36.687598	−4.677597	23.49	2.049 ± 0.005	E	A
593	36.698937	−4.700375	23.51	2.164 ± 0.005	E	A
117	36.689081	−4.681802	23.52	1.474 ± 0.005	E	A
177	36.672820	−4.685007	23.65	0.798 ± 0.005	E	A
156	36.694895	−4.684186	23.66	1.965 ± 0.005	E	A
504	36.690690	−4.697156	23.79	1.064 ± 0.005	E	B
477	36.700287	−4.696110	23.82	1.833 ± 0.005	E	B
332	36.671646	−4.691251	23.83	1.785 ± 0.005	E	B
21	36.681790	−4.673701	23.88	1.489 ± 0.005	E	A
39	36.689767	−4.675155	23.94	2.047 ± 0.005	E	A
282	36.669934	−4.689446	23.98	1.940 ± 0.005	E	B
145	36.665669	−4.683570	24.00	1.631 ± 0.005	E	A
149	36.679709	−4.683808	24.01	1.173 ± 0.005	E	A
175	36.698451	−4.684924	24.03	1.520 ± 0.005	E	A
538	36.683767	−4.698538	24.22	1.111 ± 0.005	E	B
427	36.671179	−4.694407	24.29	1.000 ± 0.005	E	A
677	36.670007	−4.703092	24.29	0.665 ± 0.005	E	A
742	36.678980	−4.705792	24.43	1.135 ± 0.005	E	A
581	36.691821	−4.699903	24.55	1.170 ± 0.005	E	A
598	36.688125	−4.700496	24.77	1.470 ± 0.005	E	A
87	36.687851	−4.679866	24.94	2.154 ± 0.005	E	B

TABLE 4 — *Continued*

ID	R.A.	Dec.	H_{160}	$z_{\rm grism}$	Type	Quality

NOTE. — Type 'E' and 'C' denote emission line and continuum-based grism redshifts, respectively. Uncertainties on emission line redshifts are listed as 0.005, based on our external comparison with higher-resolution data in Section 3.1; errors on the continuum-derived redshifts are based on the MCMC chains. Quality flags are explained in the text.

B. METHOD FOR FITTING OF GRISM SPECTRA AND PHOTOMETRY

`pyspecfit` is based on the MCMC sampler `MultiNest` (Feroz et al. 2009). It accepts as input one or more spectra, with associated LSFs, along with broadband photometric data. For a given set of model parameters proposed by the sampler, the likelihood $\mathcal{L}$ is computed as follows. We begin with a grid of Bruzual & Charlot (2003) simple stellar population (SSP, or "burst") models with a Salpeter (1955) IMF. First, the SSPs are interpolated to the desired metallicity and integrated over the star formation history. We adopt an exponentially declining model with SFR $\propto e^{-t/\tau}$ for $t > -t_0$, where SFR is the star formation rate at time t, τ is the e-folding time, $t = 0$ at the epoch of observation, and t_0 is the age. Gas lost during stellar evolution is not recycled. Next, dust attenuation is applied using the Calzetti et al. (2000) law, parameterized by the attenuation A_V at 5500 Å. Finally, the spectrum is redshifted, and attenuation by the intergalactic medium blueward of Lyα is taken into account following Madau (1995).

The model is then binned to the wavelength grid of each observed spectrum and convolved by the LSF (i.e., the galaxy light profile) to produce model spectra, i.e., $M^{\rm G102}$ and $M^{\rm G141}$ for the fits described in Section 3.2. The model is also integrated over the filter transmission curves to obtain the model flux density $M_k^{\rm phot}$ through each observed filter. The likelihood is $\mathcal{L} = \exp(-\frac{1}{2}\chi^2)$, where

$$\chi^2 = \sum_i \left(\frac{D_i^{\rm G102} - P(\lambda_i) M_i^{\rm G102}}{\sigma_i^{\rm G102}} \right)^2 + \sum_j \left(\frac{D_j^{\rm G141} - P(\lambda_j) M_j^{\rm G141}}{\sigma_j^{\rm G141}} \right)^2 + \sum_k \left(\frac{D_k^{\rm phot} - M_k^{\rm phot}}{\sigma_k^{\rm phot}} \right)^2 . \quad \text{(B1)}$$

Here $D^{\rm G102}$ and $D^{\rm G141}$ are the observed spectra with associated uncertainties $\sigma^{\rm G102}$ and $\sigma^{\rm G141}$, i and j run over the pixels in each spectrum, and $D_k^{\rm phot}$ is flux density measured in filter k with uncertainty $\sigma_k^{\rm phot}$. $P(\lambda)$ is a polynomial that scales and modulates the shape of the spectra. At minimum a constant is necessary to scale the spectra to the total flux, but it is also desirable to allow for some variation in the broadband spectral shape (see also Brammer et al. 2012). We use a linear $P(\lambda)$, which is continuous across the entire wavelength range spanned by both grisms, and determine the coefficients that minimize χ^2 for a given set of model parameters using a linear least-squares approach. Essentially, this procedure allows for a mild deformation of the spectral shape to match the photometric data, but the low polynomial order prevents the introduction of a spectral break.

For our fits to the spectra and photometry of the individual galaxies in our continuum sample (Section 3.2), we chose uniform priors over $1 < z < 3$, $7 < \log \tau/{\rm yr} < 10$, $8 < \log t_0/{\rm yr} < \log a(z)/{\rm yr}$, and $0 < A_V < 2$, and where $a(z)$ is the age of the universe at redshift z. The metallicity was fixed to solar. For our analysis of the continuum-normalized stacked spectra, we allow the metallicity to vary and fit simple stellar populations as described in Section 5.2. `pyspecfit` produces samples from the posterior distribution for these parameters, as well as the stellar mass M_* (including remnants) and SFR at the observation epoch. In this paper we primarily make use of the redshift and stellar mass estimates and report the median, with 1σ errors representing the 16th and 84th percentiles. We have compared our stellar mass estimates for the continuum sample of 40 galaxies to the estimates produced by `FAST`, which fits only the broadband photometry. The redshift was fixed to $z_{\rm grism}$ in `FAST`. We find that the median difference between the two mass estimates is consistent with zero, and there is no systematic trend with mass.

C. LITERATURE COMPILATION IN FIGURE 16

Here we describe our compilation of literature measurements of the variation of the stellar mass–size relation with environment used in Figure 15. For the 6 individual clusters plotted, including JKCS 041, we use the masses and radii of individual quiescent galaxies and compare these to the mean relation that we measured in the field (Equation 1). We take this field relation as a uniform basis of comparison for every cluster, since it is based on a much larger sample of field galaxies than those used in the following studies, but we note that this may introduce some systematic errors, which are estimated below. In each case, stellar masses are converted to a Salpeter IMF and a cut of $M_* > 10^{10.7}\,{\rm M}_\odot$ is applied to ensure that similar mass ranges are probed. From Papovich et al. (2012), we take the 10 UVJ–quiescent galaxies above this limit with $P_z > 0.5$ and $R_{\rm proj} < 1$ Mpc. From Zirm et al. (2012), we take the 8 photometrically-selected candidates in their Table 1; since their masses are derived using the Maraston (2005) models, we divide them by 0.69 to account for the typical offset from BC03-based masses found by Muzzin et al. (2009). From Strazzullo et al. (2013) we take the 4 "passive early-type" galaxies above our mass limit listed in their Figure 12. From Rettura et al. (2010) we take the 18 galaxies in RDCS1252.9–2927 in their Table 1. From Raichoor et al. (2011, 2012) we take the sizes and BC03-based masses of 23 galaxies in the Lynx cluster E and W. For the Rettura et al. and Raichoor et al. data, we apply a mean offsets determined by Raichoor et al. (2011) of $\Delta \log M_* = -0.05$, which includes an aperture correction (+0.06 dex) to total Sérsic magnitudes and the mean effect of including dust attenuation (−0.11 dex), which should better match our procedure.

For each cluster we compute the mean offset $\Delta \log R_e^{\rm maj}$ from Equation 1 and estimate its uncertainty as $0.23/\sqrt{N}$ dex, where N is the number of cluster members, based on the scatter in the field relation. Several sources of systematic uncertainty may affect this comparison between our field relation and independently-measured masses and sizes of cluster galaxies. First, different authors use different photometric apertures. Using `MAG_AUTO`-scaled masses for our field galaxy sample, rather scaling to the total Sérsic magnitude, produces a shift of only $\Delta \log R_e^{\rm maj} = -0.01$ dex in Equation 1, but larger offsets could apply to other data sets. Second, the inclusion with galaxies having questionable Sérsic fits can lead to shifts of ~ 0.02 dex. Third, although we have tried to harmonize stellar mass to first order by applying offsets based on the IMF and the set of stellar population models used, other differences in the priors and fitting procedure remain. Since the Papovich et al. sample overlaps our UDS data, we are able in this case to directly compare stellar mass estimates. For the 20 overlapping UVJ-quiescent galaxies with $M_* > 10^{10.7}\,{\rm M}_\odot$, we find that our $M_*^{\rm tot}$ are offset from the Papovich et al. measures by -0.05 dex, which corresponds to a shift in $\Delta \log R_e^{\rm maj}$ of $0.63 \times (-0.05) = -0.03$ dex. These uncertainties should be kept in mind pending future studies that homogeneously analyze data from an ensemble of high-z clusters.

In addition to these studies of individual clusters, we also directly quote results from 3 studies of larger samples. From Delaye et al. (2013), we take the mean mass-normalized radii in their field and cluster samples in three redshift bins from their Table 9. From Cooper et al. (2012) we take the difference in median sizes of matched galaxy samples in high- and low-density regions of the DEEP3 survey from their Figure 3. Lani et al. (2013) publish relative sizes of red galaxies in high- and low-density regions in the UDS field, broken down by mass (their Figures 5 and 6). To better compare with the above works, we average these mass-dependent measurements in each of their redshift bins, weighting by the number of galaxies in each mass bin. Only mass bins with $M_* > 10^{10.7}\,{\rm M}_\odot$ were used, after converting to a Salpeter IMF.

REFERENCES

Andreon, S. 1996, A&A, 314, 763
—. 2011, A&A, 529, L5
Andreon, S., Davoust, E., & Heim, T. 1997, A&A, 323, 337
Andreon, S., de Propris, R., Puddu, E., Giordano, L., & Quintana, H. 2008, MNRAS, 383, 102
Andreon, S., & Huertas-Company, M. 2011, A&A, 526, A11
Andreon, S., Maughan, B., Trinchieri, G., & Kurk, J. 2009, A&A, 507, 147
Atek, H., Malkan, M., McCarthy, P., et al. 2010, ApJ, 723, 104
Bassett, R., Papovich, C., Lotz, J. M., et al. 2013, ApJ, 770, 58
Bell, E. F., Papovich, C., Wolf, C., et al. 2005, ApJ, 625, 23
Bernardi, M., Hyde, J. B., Sheth, R. K., Miller, C. J., & Nichol, R. C. 2007, AJ, 133, 1741
Bertin, E., & Arnouts, S. 1996, A&AS, 117, 393
Bessell, M. S. 1990, PASP, 102, 1181
Bezanson, R., van Dokkum, P. G., Tal, T., et al. 2009, ApJ, 697, 1290
Bielby, R., Hudelot, P., McCracken, H. J., et al. 2012, A&A, 545, A23
Bielby, R. M., Finoguenov, A., Tanaka, M., et al. 2010, A&A, 523, A66
Brammer, G. B., van Dokkum, P. G., & Coppi, P. 2008, ApJ, 686, 1503
Brammer, G. B., van Dokkum, P. G., Franx, M., et al. 2012, ApJS, 200, 13
Bruce, V. A., Dunlop, J. S., Cirasuolo, M., et al. 2012, MNRAS, 427, 1666
Bruzual, G., & Charlot, S. 2003, MNRAS, 344, 1000
Buitrago, F., Trujillo, I., Conselice, C. J., et al. 2008, ApJ, 687, L61
Buitrago, F., Trujillo, I., Conselice, C. J., & Häußler, B. 2013, MNRAS, 428, 1460
Calzetti, D., Armus, L., Bohlin, R. C., et al. 2000, ApJ, 533, 682
Carollo, C. M., Bschorr, T. J., Renzini, A., et al. 2013, arXiv:1302.5115
Chabrier, G. 2003, PASP, 115, 763
Chang, Y.-Y., van der Wel, A., Rix, H.-W., et al. 2013a, ApJ, 762, 83
—. 2013b, ApJ, 773, 149
Conroy, C., Graves, G., & van Dokkum, P. 2013, arXiv:1303.6629
Cooper, M. C., Griffith, R. L., Newman, J. A., et al. 2012, MNRAS, 419, 3018
Damjanov, I., McCarthy, P. J., Abraham, R. G., et al. 2009, ApJ, 695, 101
Damjanov, I., Abraham, R. G., Glazebrook, K., et al. 2011, ApJ, 739, L44
Delaye, L., Huertas-Company, M., Mei, S., et al. 2013, arXiv:1307.0003
Dressler, A., Oemler, Jr., A., Poggianti, B. M., et al. 2013, ApJ, 770, 62
—. 2004, ApJ, 617, 867
Dressler, A., Oemler, Jr., A., Couch, W. J., et al. 1997, ApJ, 490, 577
Eisenhardt, P. R. M., Brodwin, M., Gonzalez, A. H., et al. 2008, ApJ, 684, 905
Fakhouri, O., Ma, C.-P., & Boylan-Kolchin, M. 2010, MNRAS, 406, 2267
Fan, L., Lapi, A., Bressan, A., et al. 2010, ApJ, 718, 1460
Fan, L., Lapi, A., De Zotti, G., & Danese, L. 2008, ApJ, 689, L101
Feroz, F., Hobson, M. P., & Bridges, M. 2009, MNRAS, 398, 1601
Galametz, A., Stern, D., Pentericci, L., et al. 2013, arXiv:1309.6645
Gobat, R., Rosati, P., Strazzullo, V., et al. 2008, A&A, 488, 853
Gobat, R., Daddi, E., Onodera, M., et al. 2011, A&A, 526, A133
Gobat, R., Strazzullo, V., Daddi, E., et al. 2013, arXiv:1305.3576
Grogin, N. A., Kocevski, D. D., Faber, S. M., et al. 2011, ApJS, 197, 35
Guo, Y., McIntosh, D. H., Mo, H. J., et al. 2009, MNRAS, 398, 1129
Hopkins, P. F., Bundy, K., Murray, N., et al. 2009, MNRAS, 398, 898
Huertas-Company, M., Shankar, F., Mei, S., et al. 2012, arXiv:1212.4143
Huertas-Company, M., Mei, S., Shankar, F., et al. 2013, MNRAS, 428, 1715
Jian, H.-Y., Lin, L., & Chiueh, T. 2012, ApJ, 754, 26
Kajisawa, M., Ichikawa, T., Tanaka, I., et al. 2011, PASJ, 63, 379
Kampczyk, P., Lilly, S. J., de Ravel, L., et al. 2013, ApJ, 762, 43
Kauffmann, G., White, S. D. M., Heckman, T. M., et al. 2004, MNRAS, 353, 713
Kewley, L. J., Geller, M. J., & Jansen, R. A. 2004, AJ, 127, 2002
Koekemoer, A. M., Faber, S. M., Ferguson, H. C., et al. 2011, arXiv:1105.3754
Kormendy, J., & Kennicutt, Jr., R. C. 2004, ARA&A, 42, 603
Kriek, M., van Dokkum, P. G., Franx, M., Illingworth, G. D., & Magee, D. K. 2009, ApJ, 705, L71
Kriek, M., Labbé, I., Conroy, C., et al. 2010, ApJ, 722, L64
Kümmel, M., Walsh, J. R., Pirzkal, N., Kuntschner, H., & Pasquali, A. 2009, PASP, 121, 59
Lani, C., Almaini, O., Hartley, W. G., et al. 2013, arXiv:1307.3247
Lawrence, A., Warren, S. J., Almaini, O., et al. 2007, MNRAS, 379, 1599
Le Fèvre, O., Vettolani, G., Paltani, S., et al. 2004, A&A, 428, 1043
Lin, L., Cooper, M. C., Jian, H.-Y., et al. 2010, ApJ, 718, 1158

Lotz, J. M., Papovich, C., Faber, S. M., et al. 2013, ApJ, 773, 154
Madau, P. 1995, ApJ, 441, 18
Maraston, C. 2005, MNRAS, 362, 799
McGee, S. L., Balogh, M. L., Bower, R. G., Font, A. S., & McCarthy, I. G. 2009, MNRAS, 400, 937
McGrath, E. J., Stockton, A., Canalizo, G., Iye, M., & Maihara, T. 2008, ApJ, 682, 303
McIntosh, D. H., Guo, Y., Hertzberg, J., et al. 2008, MNRAS, 388, 1537
Moran, S. M., Ellis, R. S., Treu, T., et al. 2007, ApJ, 671, 1503
Moresco, M., Pozzetti, L., Cimatti, A., et al. 2010, A&A, 524, A67
Muzzin, A., Marchesini, D., van Dokkum, P. G., et al. 2009, ApJ, 701, 1839
Muzzin, A., Wilson, G., Demarco, R., et al. 2013, ApJ, 767, 39
Muzzin, A., Wilson, G., Yee, H. K. C., et al. 2012, ApJ, 746, 188
Naab, T., Johansson, P. H., & Ostriker, J. P. 2009, ApJ, 699, L178
Nair, P. B., van den Bergh, S., & Abraham, R. G. 2010, ApJ, 715, 606
Newman, A. B., Ellis, R. S., Bundy, K., & Treu, T. 2012, ApJ, 746, 162
Nipoti, C., Treu, T., Auger, M. W., & Bolton, A. S. 2009, ApJ, 706, L86
Nipoti, C., Treu, T., Leauthaud, A., et al. 2012, MNRAS, 422, 1714
Overzier, R. A., Harris, D. E., Carilli, C. L., et al. 2005, A&A, 433, 87
Padilla, N. D., & Strauss, M. A. 2008, MNRAS, 388, 1321
Papovich, C., Momcheva, I., Willmer, C. N. A., et al. 2010, ApJ, 716, 1503
Papovich, C., Bassett, R., Lotz, J. M., et al. 2012, ApJ, 750, 93
Peng, C. Y., Ho, L. C., Impey, C. D., & Rix, H.-W. 2002, AJ, 124, 266
Peng, Y.-j., Lilly, S. J., Kovač, K., et al. 2010, ApJ, 721, 193
Pierre, M., Clerc, N., Maughan, B., et al. 2012, A&A, 540, A4
Poggianti, B. M., Aragón-Salamanca, A., Zaritsky, D., et al. 2009, ApJ, 693, 112
Poggianti, B. M., Calvi, R., Bindoni, D., et al. 2013, ApJ, 762, 77
Postman, M., Franx, M., Cross, N. J. G., et al. 2005, ApJ, 623, 721
Quadri, R. F., Williams, R. J., Franx, M., & Hildebrandt, H. 2012, ApJ, 744, 88
Raichoor, A., & Andreon, S. 2012, A&A, 543, A19
Raichoor, A., Mei, S., Nakata, F., et al. 2011, ApJ, 732, 12
Raichoor, A., Mei, S., Stanford, S. A., et al. 2012, ApJ, 745, 130
Reddy, N. A., Steidel, C. C., Fadda, D., et al. 2006, ApJ, 644, 792
Rettura, A., Rosati, P., Nonino, M., et al. 2010, ApJ, 709, 512
Salpeter, E. E. 1955, ApJ, 121, 161
Shankar, F., Marulli, F., Bernardi, M., et al. 2013, MNRAS, 428, 109
Shen, S., Mo, H. J., White, S. D. M., et al. 2003, MNRAS, 343, 978
Spitler, L. R., Labbé, I., Glazebrook, K., et al. 2012, ApJ, 748, L21
Stanford, S. A., Brodwin, M., Gonzalez, A. H., et al. 2012, ApJ, 753, 164
Stockton, A., McGrath, E., Canalizo, G., Iye, M., & Maihara, T. 2008, ApJ, 672, 146
Strazzullo, V., Gobat, R., Daddi, E., et al. 2013, arXiv:1305.3577
Szomoru, D., Franx, M., van Dokkum, P. G., et al. 2010, ApJ, 714, L244
Tanaka, M., Finoguenov, A., & Ueda, Y. 2010, ApJ, 716, L152
Tanaka, M., Toft, S., Marchesini, D., et al. 2013, ApJ, 772, 113
Taylor, E. N., Franx, M., van Dokkum, P. G., et al. 2009, ApJS, 183, 295
Thomas, D., Maraston, C., Schawinski, K., Sarzi, M., & Silk, J. 2010, MNRAS, 404, 1775
Toft, S., Franx, M., van Dokkum, P., et al. 2009, ApJ, 705, 255
Treu, T., Ellis, R. S., Kneib, J.-P., et al. 2003, ApJ, 591, 53
Treu, T., Ellis, R. S., Liao, T. X., & van Dokkum, P. G. 2005, ApJ, 622, L5
Valentinuzzi, T., Fritz, J., Poggianti, B. M., et al. 2010, ApJ, 712, 226
van der Wel, A., Rix, H.-W., Wuyts, S., et al. 2011, ApJ, 730, 38
van Dokkum, P. G., & van der Marel, R. P. 2007, ApJ, 655, 30
van Dokkum, P. G., Franx, M., Kriek, M., et al. 2008, ApJ, 677, L5
van Dokkum, P. G., Whitaker, K. E., Brammer, G., et al. 2010, ApJ, 709, 1018
Weinmann, S. M., Kauffmann, G., van den Bosch, F. C., et al. 2009, MNRAS, 394, 1213
Weinzirl, T., Jogee, S., Conselice, C. J., et al. 2011, ApJ, 743, 87
Whitaker, K. E., Kriek, M., van Dokkum, P. G., et al. 2012, ApJ, 745, 179
Whitaker, K. E., Labbé, I., van Dokkum, P. G., et al. 2011, ApJ, 735, 86
Whitaker, K. E., van Dokkum, P. G., Brammer, G., et al. 2013, arXiv:1305.1943
Williams, R. J., Quadri, R. F., & Franx, M. 2011, ApJ, 738, L25
Williams, R. J., Quadri, R. F., Franx, M., van Dokkum, P., & Labbé, I. 2009, ApJ, 691, 1879
Williams, R. J., Quadri, R. F., Franx, M., et al. 2010, ApJ, 713, 738
Wuyts, S., Labbé, I., Schreiber, N. M. F., et al. 2008, ApJ, 682, 985
Zeimann, G. R., Stanford, S. A., Brodwin, M., et al. 2012, ApJ, 756, 115
Zhang, Y.-Y., Andernach, H., Caretta, C. A., et al. 2011, A&A, 526, A105
Zibetti, S., Gallazzi, A., Charlot, S., Pierini, D., & Pasquali, A. 2013, MNRAS, 428, 1479
Zirm, A. W., Toft, S., & Tanaka, M. 2012, ApJ, 744, 181